Maximum Attainable Drag Limits for Atmospheric Entry via Supersonic Retropropulsion

Noël M. Bakhtian*
Stanford University, Stanford, CA, 94305

Michael J. Aftosmis†
NASA Ames Research Center, Moffett Field, CA, 94035

This study explores augmentation of the decelerative forces experienced during Mars entry through a flow control approach which increases aerodynamic drag, based on SRP jet manipulation of the bow shock. We develop analytic drag models based upon attainable shock physics seen in high-fidelity simulations of SRP jets. These flow models use SRP jets to recover shock losses normally associated with the strong high-Mach number bow shock on the entry vehicle. Partial recovery of stagnation pressure allows for significant deceleration at comparatively high altitudes without the burden of increased fuel mass, increasing both the mass of deliverable payloads and the payload mass fraction. To quantify achievable benefits, an analytical study determines the maximum possible drag coefficients for cascading shock structures (oblique shocks followed by a normal shock) at γ values ranging from 1.2 to 1.4. A trajectory study then quantifies the potential gains in drag during entry, along with estimates of total vehicle mass and payload mass fraction, revealing a tremendous potential for aerodynamic drag which is substantial even if only a modicum of the stagnation pressure losses can be recovered through SRP flow control. Finally, a strategy is introduced for exploiting the vast, untapped drag potential afforded via this technique. Based on these augmented drag potential values, the study establishes this nascent SRP-based flow control concept as a technology capable of satisfying the decelerative exigency of high-mass Mars entry scenarios.

Nomenclature

B	: bow shock (baseline)	m	: mass
C_A	: axial force coefficient	N	: normal shock
C_D	: drag coefficient	O	oblique shock
C_P	: coefficient of pressure	O-N	: oblique-normal shock cascade
C_T	: thrust coefficient	P, p	: pressure
D	: drag	q	: dynamic pressure
F	: force	r	: distance from planet center
$\mathcal{F}$	: function	r_{Mars}	: radius of Mars
g	: acceleration of gravity	S	: area
L	: lift	T	: thrust
M	: Mach number	t	: time
		V	: speed

ABBREVIATIONS

CFD	: computational fluid dynamics	JI	: jet interaction
DOF	: degrees of freedom	MPF	: Mars Pathfinder
DGB	: disk-gap-band	PMF	: payload mass fraction
EDL	: entry, descent, and landing	SRP	: supersonic retropropulsion

*Ph.D. Candidate, Dept. of Aeronautics and Astronautics, Durand Building, 496 Lomita Mall, Student Member AIAA.
†Aerospace Engineer, NASA Advanced Supercomputing Division, Associate Fellow AIAA.

GREEK SYMBOLS

β	: oblique shock wave angle
Γ	: flight path angle
γ	: specific heat ratio
δ	: inclination to freestream
ζ	: longitude
θ	: flow deflection angle
μ	: standard gravitational parameter
ρ	: density
ϕ	: latitude
ψ	: heading angle
ω	: planetary angular rotation rate

SUBSCRIPTS

$_{aug}$	: augmentation
$_{blend}$	: averaged cascade case
$_{eff}$	: effective
$_{max}$	: maximum
$_{n}$	: normal
$_{o}$	: stagnation
$_{ref}$	: reference
$_{t}$	: tangential
$_{x}$	: axial
$_{\infty}$	: freestream

I. Introduction

With sample-return and manned missions on the horizon for Mars exploration, the ability to decelerate high-mass systems upon arrival at a planet's surface has become a research priority. Mars' thin atmosphere necessitates the use of entry, descent, and landing (EDL) systems to aid in deceleration to sufficiently low terminal descent velocities.[1,2] Although all of NASA's Mars missions to date have utilized an EDL system based around the supersonic disk-gap-band (DGB) parachute first designed for the 1976 Viking missions, the limits of this heritage technology are being challenged by advancing mission requirements. As compared to the approximately 1-ton landed payload mass capability of the upcoming MSL mission (incorporating state-of-the-art but still incremental improvements to the Viking entry system architecture), manned missions to Mars could demand payloads of 40-100 metric tons.[3] Supersonic retropropulsion (SRP), the use of propulsive deceleration during the supersonic portion of entry (Figure 1), is currently being developed through the NASA Enabling Technology Development & Demonstration (ETDD) Program as a candidate enabling EDL technology for future high-mass Mars missions.[4]

A. Previous Work

The use of retropropulsive jets in a supersonic freestream as a means of atmospheric deceleration is a relatively new field. Proposed in several early works,[5–9] the concept resurfaced in response to the recent challenge of high-mass delivery in Mars' low-density atmosphere.[1–3,10,11] A NASA study commissioned in 2008 (Ref. 12) identified eight Exploration-class[a] EDL architectures, four of which incorporate SRP, renewing interest in and triggering the latest SRP research. This recent exploratory work includes but is not limited to[4]

- Wind tunnel testing[13–16] for CFD simulation and model development
- Validation of preliminary CFD solutions (both inviscid[17,18] and viscous[14–16,18–23]) anchored to existing experimental data (both new and historic[8,24–26])
- Parametric CFD studies examining the SRP design space[27]

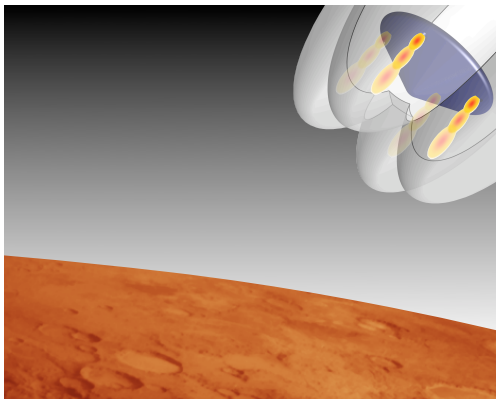

Figure 1. Illustration of SRP for atmospheric deceleration.

Prior to the recent flurry of work on SRP as a decelerative mechanism, the majority of research (overview given in Reference 28) on "counterflowing", "opposing", and "retro" jets in a supersonic freestream was performed to study drag *reduction* and concentrated on an aerospike-like[29] central, single-nozzle configuration.

[a] 10-50 metric tons of landed payload.

The most relevant historical data for the SRP community was gathered from the experiments reporting non-zero drag values, considering that the sum of thrust and drag forces on the entry vehicle are what determine the total axial force (Fig. 2) and thus the vehicle's deceleration,

$$C_A = C_T + C_D \tag{1}$$

Experimental observations made in the 1960's and early 1970's by Jarvinen and Adams,[8,24] Keyes and Hefner,[7] and Peterson and McKenzie[6] suggest that some multiple-nozzle configurations at certain conditions are capable of preserving the inherent bow shock drag, in addition to providing deceleration from thrust, thus giving some additional retroforce. Figure 3 demonstrates the drag trends established in Ref. 8, showing degrees of drag preservation at C_T values less than 3 for the peripheral nozzle configuration, and negligible drag for all C_T conditions for the central nozzle configuration, where C_T is defined as

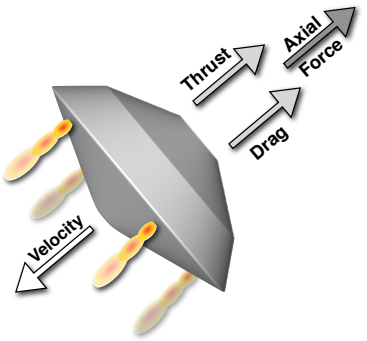

Figure 2. Thrust and drag forces contribute to the total axial force, serving to decelerate the vehicle.

$$C_T = \frac{T}{q_\infty S_{ref}} \tag{2}$$

Note that the maximum demonstrated C_D values in Figure 3 are that of the baseline (thrust off, $C_T = 0$) case.

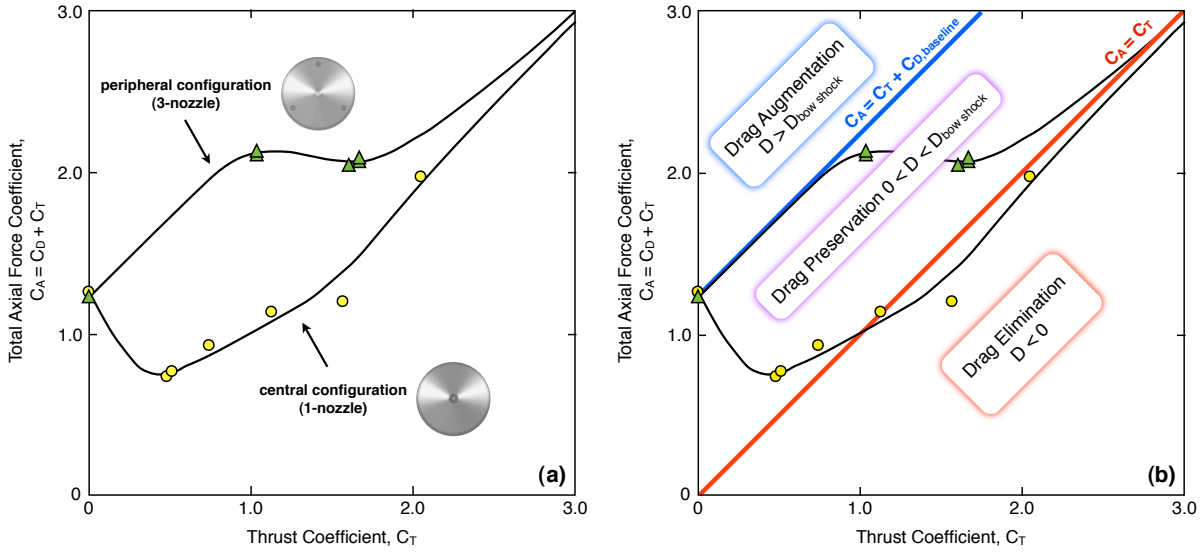

Figure 3. (a) Axial force as a function of thrust coefficient for central and peripheral nozzle SRP configurations. Experimental values and trend lines were lifted from Figures 55 and 56 of Ref. 24 and represent Mach 2 conditions at $\alpha = 0°$. (b) Overlaid red line indicates values at which $C_A = C_T$, meaning that the entire axial force is due to thrust alone and drag is zero. Blue line indicates 100% preservation of the native bow shock drag (SRP-off) in addition to the thrust force.

A number of recent systems-level studies examine landed payload mass values attainable using SRP for deceleration during atmospheric descent. A few of the earlier works assumed full drag preservation (the blue line in Figure 3) by adding a constant C_D value, the vehicle's supersonic drag coefficient, to the C_T value during the SRP burn phase of the trajectory.[30,31] References 12, 32, and 33 used a conservative no-drag model (the red line in Figure 3), using only the thrust force for deceleration during the SRP burn. Other studies account for drag preservation, utilizing a low-fidelity aerodynamic model based on the Jarvinen and Adams peripheral configuration results of Figure 3 (the points falling between the red and blue lines).[34–37] In these latter studies, the thrust force was supplemented with a percentage of the baseline drag force when thrust levels were such that $C_T < 3$. Several of these works also included a sensitivity study examining the

effect of the drag preservation value on the amount of SRP propellant mass needed; these studies focused only on low drag levels (from zero drag up to the baseline drag level in Ref. 37 and a 10% increase in Ref. 38) resulting in only a 5% increase in payload mass fraction in the first case, and less than 0.3% decrease in entry mass[b] in the second. Korzun and Braun (Ref. 35) perform a more extensive study in which drag preservation values are varied up to 200%, resulting in less than a 6% decrease in required propellant mass fraction.

Across the board, these studies demonstrated that SRP-based architectures performed poorly with respect to competing architecture technologies.[32,36,39] By requiring extremely high propellant mass fractions, EDL systems with an SRP phase experienced substantially eroded payload mass fractions (on the order of 30% PMF). In addition, the studies which utilized the fractional drag preservation model (Refs. 35 and 36) concluded that SRP benefits very little from the impact of drag preservation and that modeling a zero drag SRP burn (relying completely on thrust for deceleration) is adequate for future work.

Based on some of these systems-level studies and the low-drag trends demonstrated in the early experimental SRP work (embodied by Fig. 3), the current SRP project is moving towards a framework in which thrust (C_T in Eq. 1) is the dominant contribution to deceleration.[4] This paper focuses on an alternative SRP-based approach to the substantial deceleration required for human Mars exploration - rather than emphasize the thrust, we concentrate on augmenting the aerodynamic drag on the entry body (C_D in Eq. 1) using favorable interactions from the SRP jets. Note that in the studies discussed above, 100% drag "preservation" constitutes maintaining only the native aerodynamic drag of a thrust-off configuration (drag inherent in bow shock physics). The focus of this paper is drag augmentation, or increasing the drag coefficient value above that baseline level (above the blue line in Fig. 3). Introduced in Ref. 27, percentage C_D augmentation is defined in this work as

$$C_{Daug} = \frac{C_D - C_{D,ref}}{C_{D,ref}} \times 100\% \tag{3}$$

where the reference C_D value is the drag coefficient experienced with thrust off ($C_T = 0$) at the same windspace conditions. With this definition, elimination of all drag results in $C_{Daug} = -100\%$, preserving 100% of the baseline drag (100% drag preservation) gives $C_{Daug} = 0\%$, and doubling the baseline SRP-off drag gives $C_{Daug} = 100\%$.

It is axiomatic that any increase in deceleration through drag reduces the thrust requirements of SRP, saving propellant mass and increasing payload mass; the remainder of the study assumes full reliance on the drag force for deceleration.

B. Drag Augmentation Model

In Reference 27, we introduced a novel mechanism for significant drag augmentation through favorable jet interaction (JI) in SRP flows. The flow model describing the drag augmentation mechanism, shown in Figure 4, relies on shock manipulation of the capsule's bow shock. The bow shock is a key decelerative physical mechanism due to the post-shock pressure increase; however, stagnation losses through this shock also severely reduce the maximum recoverable pressure on the body, thus drastically limiting the potential for producing large amounts of drag. For example, in $\gamma = 1.4$ conditions at $M_\infty = 6$, the stagnation pressure behind a normal shock has decreased to less than 3% of its initial value ($P_{o,N}/P_{o1} = 0.02965$), implying that the maximum recoverable pressure has dropped by 97%. Recognizing this, the current study seeks to exploit the available reservoir of potential drag by altering the flow physics of the system through the use of retropropulsive jets as oblique shock generators.

As described in Reference 27, supersonic plumes behave in a manner similar to "hard" geometry. As the plume penetrates the supersonic freestream, a bow shock system forms about the effective body, wrapping around the jet plume as seen in Figure 4a. The skirt of this plume-shock is oblique to the oncoming flow, and freestream flow passing through the oblique section is compressed without experiencing the massive stagnation pressure losses of an entry-velocity normal shock ($P_{o2,O} > P_{o2,N}$).

In this way, portions of the capsule face surface can be protected from stagnation pressure losses by the oblique shock skirts of the plume-shocks. Moreover, interaction regions between adjacent plume-shock skirts lead to oblique shock-shock interactions (Figure 4b), further decelerating the oncoming flow and raising the pressure incrementally through cascading oblique shock compressions. This incremental flow deceleration

[b]The first study (Ref. 37) keeps mass at atmospheric entry constant and allows propellant and payload masses to change while the second (Ref. 38) fixes payload mass and optimizes for minimum entry mass.

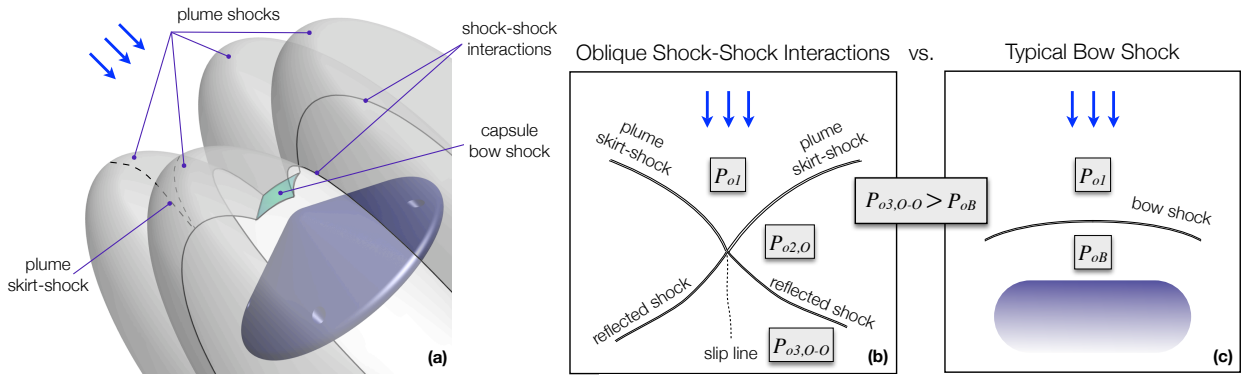

Figure 4. Flow model for drag augmentation. a) Diagram showing plume-shocks resulting from retro-plumes (not pictured). Solid lines indicate shock-shock interactions, including oblique interactions between adjacent plume-shock skirts. b) A two-dimensional diagram representing a slice through adjacent plume-shock skirts showing the interaction between two plume skirt-shocks (indicated by dotted lines in (a)). The resulting stagnation pressure $P_{o3,O\text{-}O}$ is contrasted with c) the stagnation pressure behind a bow shock $P_{o,B}$.

technique allows significant preservation of freestream stagnation pressure, enabling higher surface pressures and, ultimately, drag augmentation, as seen in Figure 5.

This paper offers a preliminary quantification of the potential benefits of shock manipulation via SRP jets. Through an analytic study of attainable pressures by way of different shock structures, we determine maximum drag coefficient values possible with this method of SRP-based flow control. Utilizing these C_D profiles, a trajectory study gives bounds on drag values and allows estimation of maximum payload masses, establishing the feasibility of flow control via SRP as a Mars EDL technology.

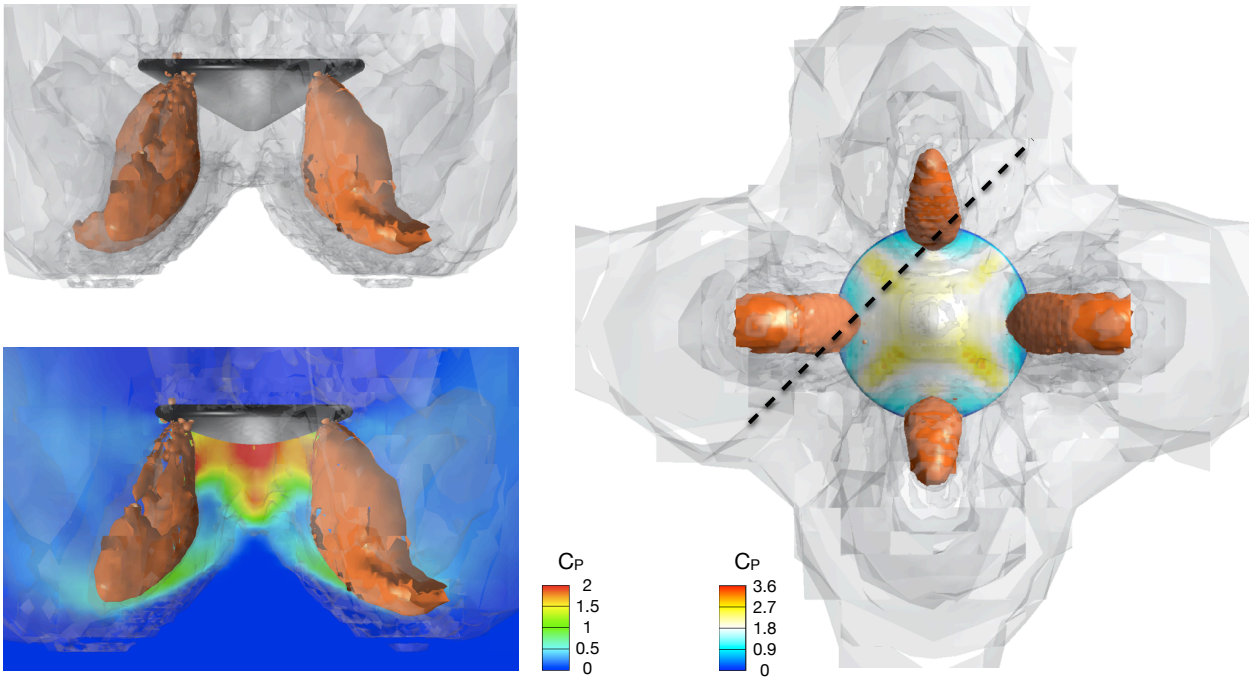

Figure 5. Three-dimensional representation of the plume-shocks (gray) wrapping around each jet (orange), the pressure on a diagonal cutting-plane intersecting two adjacent nozzles, and an axial view showing the surface pressure coefficient with a yellow "X" overpressure pattern due to shock-shock interactions of the plume-shock skirts (results from the parametric study in Ref. 27).

II. Approach and Validation

Preliminary studies have proven the potential for drag augmentation from shock manipulation upwind of an entry capsule, however the feasible extent of these augmentation levels is an unknown. This work seeks to establish realistic upper bounds for C_D and drag based on flow control via SRP jets.

In the following analysis, we relate C_D simply and directly to a nominal pressure value and study the drag potential offered by different shock structures solely by concentrating on post-shock flow pressures. The simplest shock structure analyzed in this work is the flow through a normal shock, which serves as a starting point for a bow shock approximation. We then concentrate on the drag potential of different shock cascades in which the freestream flow traverses multiple shocks. Figure 4b illustrates how SRP jets can produce these oblique shock cascade, and Figure 5 shows results of numerical studies on a simple jet configurations which produced this jet interaction mechanism for real SRP flow.[27] More complex jet geometries could result in extensive shock cascade structures.

Section IIA notes the assumptions made to complete the analytic C_D study and describes the method and terminology, and Section IIB provides validation of this analytic method against experimental and CFD data.

A. Analytical Method and Assumptions

To compare the drag benefits of different shock structures, we require a simplified C_D model based solely on post-shock pressures. Starting with the drag definition

$$D = \int p \, dS_x \tag{4}$$

where S_x is the projection of the local area normal in the streamwise direction, and taking p_{front} and p_{back} to be the mean pressures on the front and back faces of the geometry,

$$D = p_{front} S_{front,x} - p_{back} S_{back,x} \tag{5}$$

Using the standard definition of C_D,

$$C_D = \frac{D}{q_\infty S_{ref}} \tag{6}$$

and taking reference area to be the projected area, $S_{ref} = S_{front,x} = S_{back,x}$ gives

$$C_D = \frac{p_{front} - p_{back}}{q_\infty} \tag{7}$$

A vacuum on the back face ($p_{back} = 0$) results in the highest pressure differential and thus largest drag on the body, but at the atmospheric conditions being considered, pressure is so low that an assumption of $p_{back} = p_\infty$ is both suitable and more conservative. This substitution allows the approximation

$$C_D \approxeq \frac{p_{front} - p_\infty}{q_\infty} \tag{8}$$

Recalling the pressure coefficient definition

$$C_P = \frac{p - p_\infty}{q_\infty} \tag{9}$$

we note that the right-hand side of Equation 8 gives exactly $C_{P,front}$, a C_P value based on the mean pressure on the front face of the geometry. In this way, the drag coefficient can now be evaluated simply through computing a representative face pressure. In our estimations of drag coefficient based on various structures, we assume that all flow prior to the geometry has traversed through the same shock structure and yields a constant pressure on the front face (Fig. 6), allowing us to use the post-shock pressures for p_{front} in Equation 8, or more simply

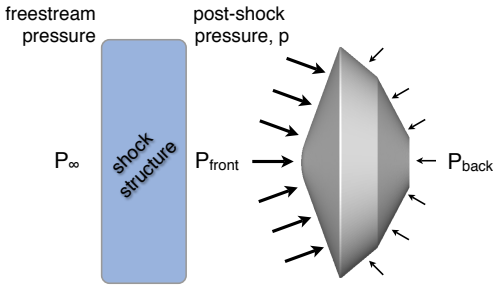

Figure 6. Mean pressure on the front face is evaluated as the final flow pressure subsequent to shock processing.

$$C_D = C_P = \frac{p - p_\infty}{q_\infty} = \frac{p - p_\infty}{\frac{1}{2}\gamma p_\infty M_\infty^2} = \frac{\frac{p}{p_\infty} - 1}{\frac{1}{2}\gamma M_\infty^2} \tag{10}$$

Here, p is the post-shock pressure and a useful surrogate for the mean pressure on the capsule face (Fig. 6).

The drag coefficient for each SRP shock structure in the study can now be computed with Equation 10, where the pressure ratio $\frac{p}{p_\infty}$ is that of the entire shock structure. As discussed in Section IB, the stagnation pressure behind a high-Mach normal shock ("N") is insubstantial and results in limited drag values, but this loss can be mitigated by adding an oblique shock ("O") prior to the normal shock, creating a shock cascade ("O-N"). Increasingly complex shock cascades are analyzed, each terminating in a normal shock and thus guaranteeing subsonic flow at the surface. For each cascade shock structure, the ratio $\frac{p}{p_\infty}$ takes into account processing by all shocks.

Both stagnation and static post-shock pressures are used in the analysis, and the resulting drag coefficients are denoted as C_{Do} and C_D, respectively, where

$$C_{Do} = C_{Po} = \frac{\frac{p_o}{p_\infty} - 1}{\frac{1}{2}\gamma M_\infty^2} \tag{11}$$

and

$$C_D = C_P = \frac{\frac{p}{p_\infty} - 1}{\frac{1}{2}\gamma M_\infty^2} \tag{12}$$

The freestream stagnation pressure, representing the absolute maximum recoverable pressure, establishes an absolute drag limit. Thus, the actual reported maximum drag coefficient values will all be based on the C_{Do} calculated behind each shock structure. Figure 7 illustrates the cascade terminology used throughout the work.

Shock Structure	Abbreviation	P_∞		post-shock 1		post-shock 2		post-shock 3		drag coefficient	
		static	stagnation	static	stagnation	static	stagnation	static	stagnation	static	stagnation
P_1 S1 P_2 B	B	P_1	P_{o1}	P_B	P_{oB}					$C_{D,B}$	$C_{Do,B}$
P_1 S1 P_2 N	N	P_1	P_{o1}	$P_{2,N}$	$P_{o2,N}$					$C_{D2,N}$	$C_{Do2,N}$
P_1 S1 O S2 N P_3	O-N	P_1	P_{o1}	$P_{2,O}$	$P_{o2,O}$	$P_{3,O\text{-}N}$	$P_{o3,O\text{-}N}$			$C_{D3,O\text{-}N}$	$C_{Do3,O\text{-}N}$
P_1 S1 O S2 O S3 N P_4	O-O-N	P_1	P_{o1}	$P_{2,O}$	$P_{o2,O}$	$P_{3,O\text{-}O}$	$P_{o3,O\text{-}O}$	$P_{4,O\text{-}O\text{-}N}$	$P_{o4,O\text{-}O\text{-}N}$	$C_{D4,O\text{-}O\text{-}N}$	$C_{Do4,O\text{-}O\text{-}N}$
⋮											⋱

Figure 7. Shock structure terminology for multiple shock (S) structures. Stagnation drag coefficients, C_{Do}, represent the maximum drag coefficient values. P_{blend}, not listed here, represents an average of the N, O-N, and O-O-N cases (Eqn. 27).

B. Validation of the Analytical Model

To validate the analytical model, we compare analytic estimates of C_D with both computational and experimental results of blunt body flows decelerated by a bow shock. The experimental values taken from Ref. 40 represent C_D on the front face of a blunt-face object and a flat-faced short body in supersonic flow.[40] Numerical results were computed using the CART3D package, a parallel Cartesian-based Euler solver with adaptive mesh refinement.[41–45] We report C_D on the front face[c] of a Viking aeroshell (half-angle of 70° as shown in Fig. 8) at $\alpha = 0°$ over a Mach range of 1.1 to 10. Finally, analytic estimates of C_D were generated following the method of Section IIA. Figure 9 compares the analytic C_D values based on the static pressure behind a normal shock ($C_{D2,N}$), static pressure

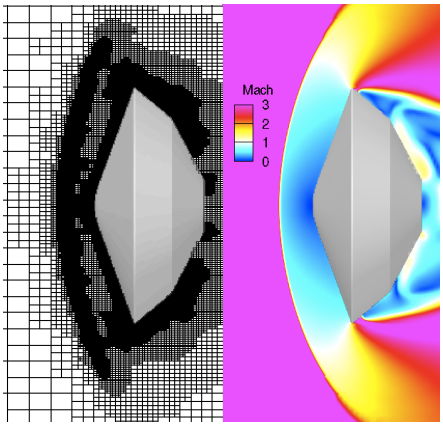

Figure 8. Cart3D mesh and solution for Viking aeroshell at Mach 4.0, γ 1.4, and $\alpha = 0°$.

[c] C_D for an individual component is calculated using C_P values based on p_∞, so reported C_D on the front face component is directly comparable with the analytical C_D for the entire body due to the back face p_∞ assumption.

behind an oblique shock ($C_{D2,O}$ at nominal β of 75°), and stagnation pressure behind a normal shock ($C_{Do2,N}$) against the numerical and experimental data points.

Comparing the experimental and CFD data in Figure 9, higher experimental drag values are expected due to the geometry of the test objects: the flat faces in the experiments will experience flatter bow shocks than the conical capsule face solutions that were computed. At high Mach numbers, the numerical limiting value compares closely with the analytic $C_{D2,O}$ curve as expected due to the high curvature of the bow shock. Below $M_\infty = 6$, the CFD data trends higher towards the analytic $C_{D2,N}$ curve, indicating the increase in pressure behind the bow shock as the oblique sections of the bow shock straighten with decreasing M_∞. At lower Mach numbers, the numerical data exhibits higher comparative C_D values as the stagnation region on the capsule face increases in area. Analytic and numerical results were also compared at various γ values and experienced a similar increase in drag coefficient with decreasing γ. Overall the analytic solutions match the characteristics seen in the experimental and computational data, validating use of our analytical method to study the drag potential of shock manipulation via SRP.

After determining the analytical C_D values for various shock structures, we quantify the possible C_D augmentation due to SRP shock manipulation by comparing against a typical entry bow shock structure. In the analyses which follow, a fraction of the the analytic C_{Do} due to a normal shock structure is used as an approximation of the bow shock drag. This approximation is based on modified-Newtonian theory,

$$C_P = C_{P,max} \sin^2 \delta \tag{13}$$

where $C_{P,max} = C_{Po2,N}$. To estimate the constant factor $\sin^2 \delta$, we take C_D based on the CFD solutions and divide by the analytic $C_{Po2,N}$. Figure 10 shows this factor to be fairly constant across a range of freestream Mach numbers. Based on the value of the multiplicative factor at $M_\infty = 10$, the remainder of this study uses the following baseline analytic approximation for a bow shock:

$$C_{D,B} = 0.851 C_{Do2,N} \tag{14}$$

Note that the analytic $C_{D,B}$ values are slightly greater than the CFD bow shock values at lower Mach numbers, meaning that drag augmentation values will be conservative in that Mach region.

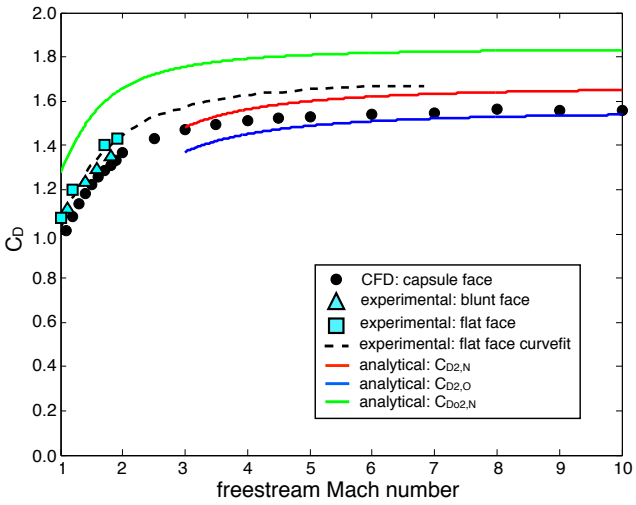

Figure 9. C_D comparisons (γ 1.4) between analytical, numerical, and experimental results. Experimental data for a blunt-face object and flat-face short body were lifted from Figures XVI-8 and XVI-14 of Ref. 40, respectively.

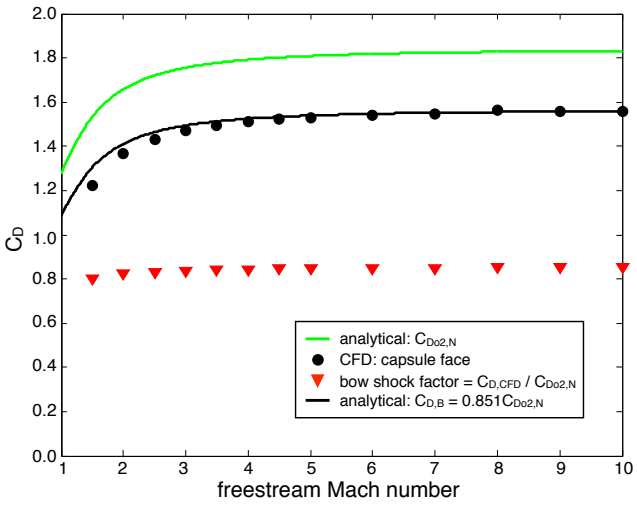

Figure 10. Determination of analytic baseline $C_{D,B}$ for a Viking-like aeroshell.

III. Results and Discussion

C_D augmentation due to shock manipulation via SRP jets is approximated using an analytic method in Section IIIA. By establishing specific entry trajectories in Section IIIB, we then determine corresponding drag values for each shock structure. Finally, maximum vehicle mass and estimated payload mass benefits are computed for SRP systems based on flow control for drag augmentation. Section IIIC establishes the potential of this technology based on the the decelerative forces required for future high-mass Mars missions.

A. Drag Coefficient Augmentation

This section culminates in C_D profiles as a function of Mach number and specific heat ratio for various shock structures. IIIA.1 works through the basic shock structures for γ 1.4, presenting analytic results for drag coefficient and the limiting (high-Mach) solutions. C_D curves are then analyzed and compared. IIIA.2 extends the discussion to lower specific heat ratios, and an atmospheric entry γ model allows a comparison of the effect of SRP shock structures on C_D in a Mars entry scenario.

1. C_D Trends for $\gamma = 1.4$

Before progressing to shock structure analysis, we note that the loss of stagnation pressure through shocks severely reduces the maximum ceiling on recoverable pressure and thus maximum drag (Eqn. 8). It follows that an isentropic (shock-free) deceleration of the flow to the surface would result in no stagnation pressure loss, yielding the maximum pressure on the surface and thus the highest possible C_D values. This maximum drag value resulting from isentropic deceleration can be computed by substituting the isentropic pressure ratio

$$\frac{P_{o,\infty}}{P_\infty} = \left(1 + \frac{\gamma - 1}{2} M_\infty^2\right)^{\frac{\gamma}{\gamma-1}} \tag{15}$$

into Eqn. 11 and taking the limit as Mach number approaches infinity,

$$\lim_{M_\infty \to \infty} C_{D,max(isentropic)} = \lim_{M_\infty \to \infty} C_{Do,\infty} = \frac{2}{\gamma}\left(\frac{\gamma+1}{2}\right)^{\frac{\gamma}{\gamma-1}}\left(M_\infty\right)^{\frac{2}{\gamma-1}} = \infty \tag{16}$$

For γ 1.4, this result scales as M_∞^5: drag coefficient values as high as 30 are reached at Mach 5, and staggering values on the order of 600 can be attained at Mach 10. The infinite limit represents a huge reserve of stagnation pressure that we can convert to drag by reducing shock losses.

As discussed in Section IIB, the drag coefficient due to a bow shock structure typical in capsule entry scenarios is approximated in this work as a fraction of the stagnation pressure behind a normal shock. Utilizing the normal shock equations for post-shock Mach number and pressure ratios (Equations 36-38 in Appendix B), the analytical maximum drag value behind a normal shock is given as a function of freestream Mach number and γ:

$$C_{D,max(N)} = C_{Do2,N} = \frac{\frac{P_{o2,N}}{P_\infty} - 1}{\frac{1}{2}\gamma M_\infty^2} = \frac{\frac{P_{o2,N}}{P_{2,N}}\frac{P_{2,N}}{P_\infty} - 1}{\frac{1}{2}\gamma M_\infty^2} = \frac{\left(1 + \frac{\gamma-1}{2}M_2^2\right)^{\frac{\gamma}{\gamma-1}}\left(1 + \frac{2\gamma}{\gamma+1}(M_\infty^2 - 1)\right) - 1}{\frac{1}{2}\gamma M_\infty^2} \tag{17}$$

where M_2 is given in Equation 36. The upper bound C_D value possible behind a normal shock occurs at limiting Mach numbers and is calculated as

$$\lim_{M_\infty \to \infty} C_{D,max(N)} = \frac{4}{\gamma+1}\left(\frac{(\gamma-1)^2}{4\gamma} + 1\right)^{\frac{\gamma}{\gamma-1}} \tag{18}$$

Similar calculations can be performed to provide drag coefficients based on static pressure rather than stagnation pressure (Eq. 12):

$$C_{D2,N} = \frac{\frac{P_{2,N}}{P_\infty} - 1}{\frac{1}{2}\gamma M_\infty^2} = \frac{4}{\gamma+1}\frac{(M_\infty^2 - 1)}{M_\infty^2} \tag{19}$$

$$\lim_{M_\infty \to \infty} C_{D2,N} = \frac{4}{\gamma+1} \tag{20}$$

Now we analytically determine the maximum drag value behind an oblique shock cascade, with flow decelerating first through an oblique shock (assuming $\beta = 31°$) and then a normal shock, resulting in an O-N cascade.

$$C_{D,max(O\text{-}N)} = C_{Do3,O\text{-}N} = \frac{\frac{P_{o3,O\text{-}N}}{P_\infty} - 1}{\frac{1}{2}\gamma M_\infty^2} = \frac{\frac{P_{o3,O\text{-}N}}{P_{3,O\text{-}N}}\frac{P_{3,O\text{-}N}}{P_{2,O}}\frac{P_{2,O}}{P_\infty} - 1}{\frac{1}{2}\gamma M_\infty^2} \tag{21}$$

Utilizing the oblique shock relations (Eqns. 39-44 in Appendix B) and Equation 21, the upper bound on C_D values behind an O-N cascade (at the Mach limit) is

$$\lim_{M_\infty \to \infty} C_{D,max(O\text{-}N)} = \frac{4}{\gamma+1}\sin^2(\beta)\left(1 + \frac{2\gamma}{\gamma+1}\left(\frac{\gamma-1}{2\gamma\tau} - 1\right)\right)\left(1 + \frac{\gamma-1}{2}\left(\frac{1 + \frac{\gamma-1}{2}\sigma^2}{\gamma\sigma^2 - \frac{\gamma-1}{2}}\right)\right)^{\frac{\gamma}{\gamma-1}} \tag{22}$$

where

$$\sigma = \left(\frac{\gamma-1}{2\gamma}\right)^{\frac{1}{2}} \frac{1}{\sin\left(\beta - \tan^{-1}\left(\frac{2\cot\beta\sin^2\beta}{\gamma+\cos(2\beta)}\right)\right)} \tag{23}$$

and

$$\tau = \sin^2\left(\beta - \tan^{-1}\left(\frac{2\cot\beta\sin^2\beta}{\gamma+\cos(2\beta)}\right)\right) \tag{24}$$

Calculating C_D based on static pressure results in

$$\lim_{M_\infty \to \infty} C_{D3,O\text{-}N} = \frac{4}{\gamma+1}\sin^2(\beta)\left(1 + \frac{2\gamma}{\gamma+1}\left(\frac{\gamma-1}{2\gamma\tau} - 1\right)\right) \tag{25}$$

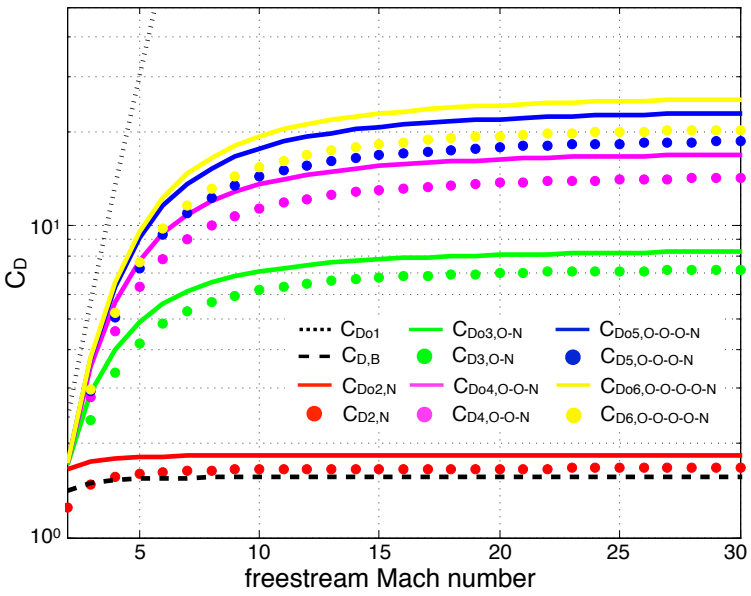

Figure 11. Analytical C_D profiles as a function of freestream Mach number at γ 1.4 with solid lines representing stagnation-based values and dotted lines representing static values.

For more complex cascade structures, we use a numerical script to analyze the trends and approximate drag limits. Figure 11 shows C_D profiles as a function of M_∞ for a normal shock and oblique-normal shock cascades ($\beta = 31°$), with both stagnation (solid) and static (dotted) curves clearly reaching limiting values. In addition, the baseline $C_{D,B}$ curve is denoted with a dashed black line for comparison, and the ultimate isentropic limit is denoted with a dotted black line.

Examining Figure 11 which shows drag coefficient values (logarithmic) as a function of Mach number at γ 1.4, we can make several observations. First, C_D values increase but level off with increasing freestream Mach number as the shocks get stronger. This is promising for SRP because higher drag coefficients will be attainable during the high-Mach portion of entry for much needed deceleration. Second, the addition of

additional oblique shocks to the shock structure results in higher C_D values at each Mach number. Although normal shocks produce higher static pressures than oblique shocks, this comes at the price of severe stagnation pressure depletion (compare red and black solid vs. dotted lines in Fig. 12). Deceleration through a shock cascade (O-N) results in a weaker normal shock, allowing higher overall stagnation and thus maximum pressure values (green lines), and generating higher drag coefficients. Finally, we note the more complex cascades in Figure 11 experience diminished returns, implying that the majority of benefit in C_D can be accrued through a simple O-N or O-O-N cascade.

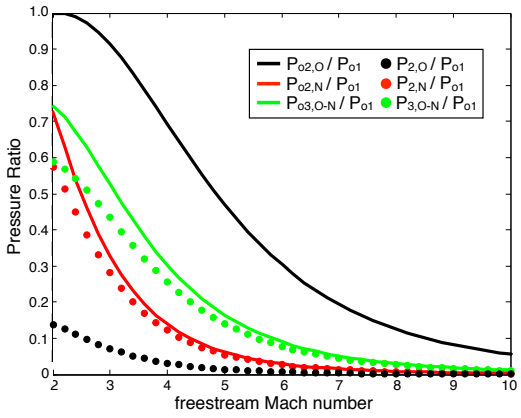

Figure 12. Pressure ratios for O, N, and a cascading O-N case.

In order to quantify the potential benefits of shock manipulation for drag augmentation, we compare analytical C_{Do} values for several shock structures against the baseline $C_{D,B}$, which is used as an approximation of the drag due to a bow shock (Eqn. 14). Maximum C_D augmentation for each shock structure is calculated using Eqn. 3 where

$$C_{D,ref} = C_{D,B} \tag{26}$$

A "blended" shock structure is also included in the results as a modest realizable case based on the flow physics of Fig. 4, and assumes that the pressure face of the vehicle experiences flow having passed through a normal shock, O-N cascade, and O-O-N cascade in equal parts such that

$$C_{Do,blend} = \frac{1}{3}\left(C_{Do2,N} + C_{Do3,O\text{-}N} + C_{Do4,O\text{-}O\text{-}N}\right) \tag{27}$$

Results are fully tabulated in Appendix C and summarized here in Table 1. The benefits at low Mach numbers are insubstantial for all shock structures, with a maximum possible augmentation from isentropic deceleration of less than 100% at $M_\infty = 2$, and corresponding values of around 20% augmentation for the small cascades. At higher Mach numbers, the C_D augmentation potential is significant - by creating an O-O-N shock structure, C_D values can be augmented more then 750% at $M_\infty = 10$, reaching values above 10, and the blended shock case experiences augmentation values close to 400%.

Table 1. Representative maximum C_D and corresponding C_{Daug} values at γ 1.4 and 1.2. Full results listed in Table 6.

γ	C_D and C_{Daug}	$M_\infty = 2$	$M_\infty = 5$	$M_\infty = 10$	$M_\infty = \infty$
1.4	$C_{Do,B}$	1.41	1.54	1.56	1.57
	C_{Do1}	2.44	30.18	606.26	∞
	$C_{Do4,O\text{-}O\text{-}N}$	1.73	7.70	13.52	17.37
	$C_{Do,blend}$	1.70	4.81	7.49	9.20
	$C_{Daug,O\text{-}O\text{-}N}$	23%	400%	768%	1010%
	$C_{Daug,blend}$	21%	212%	380%	488%
1.2	$C_{Do,B}$	1.45	1.60	1.62	1.63
	C_{Do1}	2.72	122.48	29526.00	∞
	$C_{Do4,O\text{-}O\text{-}N}$	1.80	13.19	34.20	56.13
	$C_{Do,blend}$	1.76	7.17	15.87	24.59
	$C_{Daug,O\text{-}O\text{-}N}$	24%	726%	2013%	3352%
	$C_{Daug,blend}$	21%	349%	880%	1412%

2. *Effect of γ*

From the analysis in the previous section (Eqns. 17 and 21 specifically), it's obvious that the maximum drag coefficients for each shock structure are dependent on the specific heat ratio, γ. Figure 13 shows this effect for $\gamma = \{1.2 - 1.4\}$ behind various shock cascades as compared to the baseline bow shock structure.

The maximum drag coefficient for each shock structure type is shown to be heavily dependent on γ, especially for more complex cascade structures and at higher freestream Mach number. In all cases, lower γ values lead to higher C_D values, increasing the potential payoff at high Mach numbers where real-gas effects are more prominent. For example, for an O-O-N structure at Mach 10, C_{Daug} is 768% for γ of 1.4, and 2013% for γ of 1.2, an increase of more than 2.5 times (Table 1). Appendix C gives results for each shock structure at γ values of 1.2, 1.3, and 1.4.

Having quantified the importance of specific heat ratio in the C_D calculations, we now examine the C_D trends in a sample atmospheric entry with changing γ. As an estimate, we use a constant "effective gamma", γ_{eff}, allowing the use of the simple closed-form results derived above.[46] In the results which follow, we use the following γ_{eff} values for a Mars entry trajectory, as justified in Appendix D:

$$\begin{cases} \gamma_{eff} = 1.3 & \text{if } M_\infty \leq 5 \\ \gamma_{eff} = 1.2 & \text{if } M_\infty > 5 \end{cases} \tag{28}$$

Figure 14 depicts the downward shift in drag coefficient due to the change of γ over the trajectory as the vehicle passes through Mach 5. The actual change in γ would be less immediate than this shift at $M_\infty = 5$, resulting in a smooth C_D transition, but this plot throws into sharp relief the notion that the variation of γ over the trajectory serves to further increase the effectiveness of any SRP shock manipulation tactics early in the trajectory (at higher M_∞).

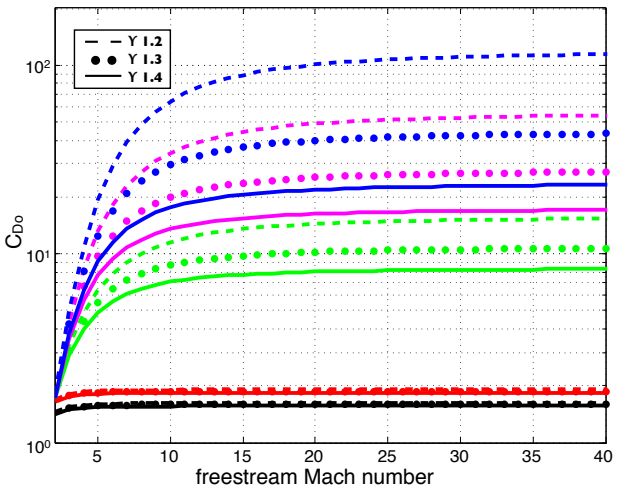

Figure 13. Maximum analytical C_D values at γ 1.2, 1.3, and 1.4 as compared to the baseline drag coefficient (black). The color scheme for cascading shocks duplicates that in Fig. 11.

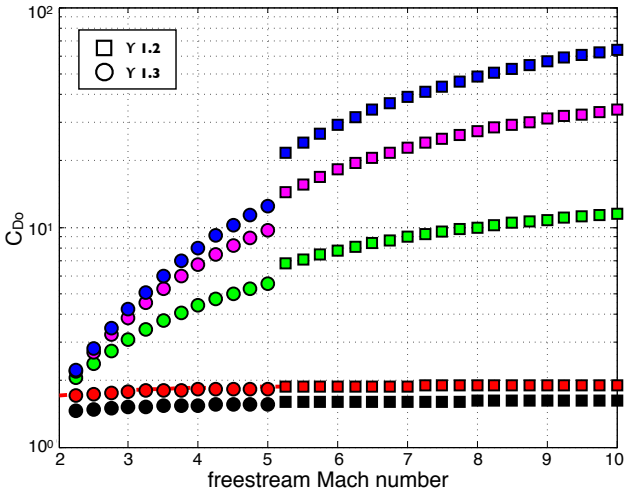

Figure 14. Maximum analytical C_D values as compared to the baseline drag coefficient (black) using γ_{eff} for a sample atmospheric entry at Mars (Eqn. 28). The color scheme for cascading shocks duplicates that in Fig. 11.

B. Drag and Mass Benefits

From the analytical drag coefficient models in the preceding section, we can now estimate corresponding drag and mass limits for SRP-based EDL systems. As conveyed in Figure 11, the drag coefficients achieved based on SRP shock manipulation are dependent on freestream Mach number, M_∞. In addition, the drag force decelerating the entry vehicle

$$D = C_D q_\infty S_{ref} \tag{29}$$

is a function of freestream dynamic pressure, q_∞. Dependencies of M_∞ and q_∞ on altitude and velocity are shown in Figure 15, highlighting the fact that information about the specific trajectory (altitude versus velocity) is required in order to calculate drag values and resulting feasible vehicle mass values.

Trajectories are calculated using the 3-DOF trajectory code described in Appendix A. In order to compare against a successful Mars mission, we utilize the Mars Pathfinder (MPF) initial conditions found in Table 5 (Appendix A) and all assumptions found in the accompanying description, including an aeroshell diameter of $2.65m$ and a constant vehicle mass over the trajectory. For the following analyses, however, C_D is no

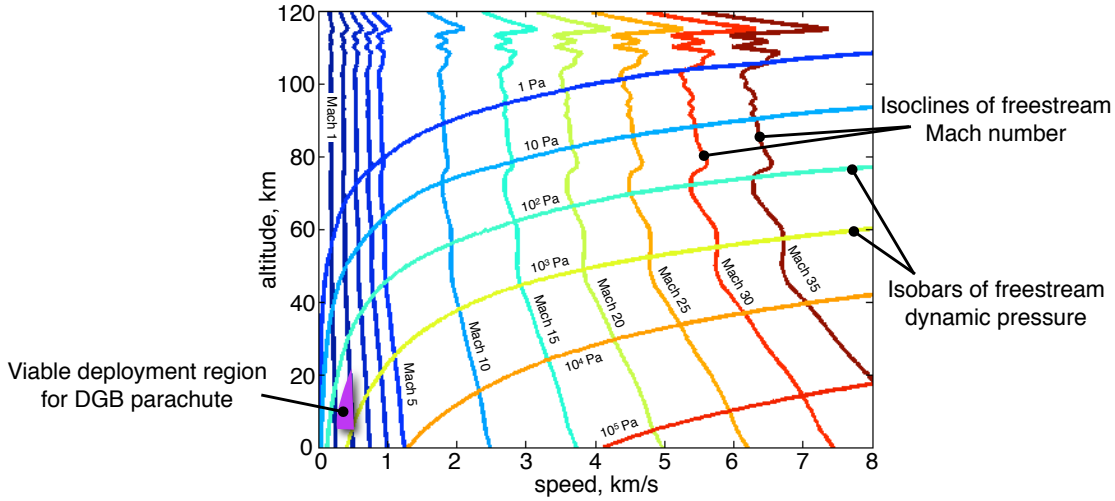

Figure 15. Contour lines of freestream Mach number and dynamic pressure in altitude-velocity space for γ 1.3 using tabulated Mars atmospheric p and ρ from Ref. 47. The termination region is illustrated in purple.

longer assumed constant; C_D is now allowed to vary along the trajectory as the freestream Mach number changes, with values based on the analytic results for each shock structure and γ from Section IIIA.

For these simulations, we assume an entry and descent system consisting of SRP followed by use of a supersonic parachute. Thus, the SRP trajectory termination criteria is based on the deployment constraints of a DGB parachute. This viable-deployment region is bounded by freestream Mach values of 2.1 and 1.1, dynamic pressure limits of $250Pa$ and $1200Pa$, and a $5km$ minimum altitude to allow for a typical descent timeline to the ground.[2] For each case, the mass limit is the maximum total vehicle mass which results in a trajectory capable of passing through this region[d] (shaded in Figure 15). To gain a better understanding of the drag trends resulting from the C_D augmentation provided through SRP shock manipulation, Section IIIB.1 first examines results from a specific shock structure: O-O-N at γ 1.2. Section IIIB.2 then compares data resulting from the entire range of shock structures and γ conditions.

1. *Drag Trends Resulting from Prescribed C_D Profiles*

To detail the trends in drag, trajectories, and feasible mass, three C_D curves ($\gamma = 1.2$) are chosen for comparison: the oblique-oblique-normal shock cascade[e] ($C_{Do4,O\text{-}O\text{-}N}$), the analytic baseline approximation of a bow shock ($C_{D,B}$), and a constant-C_D case based on the Mars Pathfinder (MPF) drag coefficient[f]. These C_D trends, discussed in Section IIIA, are illustrated in Figures 16(a-c) as C_D contours in altitude-velocity space overlaid with the maximum mass trajectories for each case plotted in white. Figure 16a portrays the MPF case with a constant C_D of 1.7025. The slightly varying C_D of the baseline case is shown in Figure 16b, exhibiting comparatively lower C_D values across the space. Finally, Figure 16c illustrates the shock cascade case (note the extended colormap ranging to values in excess of 50) exhibiting a variation with Mach number consistent with the C_D trends of Figure 13 and Mach contour lines of Figure 15. Actual C_D values over the trajectory for each case can be compared in the logarithmic Figure 17d, emphasizing the difference in C_D magnitudes especially at mid- to high altitudes.

Drag trends in altitude-velocity space are illustrated as contours in Figure 16(d-f) and are related to the C_D contours by Eqn. 29. Note the logarithmic contour scale ranging over 11 orders of magnitude. Concentrating first on the constant-C_D MPF case (Fig. 16d), the contour pattern is directly related to the q_∞ contours of Figure 15, exhibiting highest values in the high-q_∞ regions of the space (high speed, low altitude). The varying C_D cases exhibit similar drag map characteristics; however, for the shock cascade

[d]Due to the γ dependency when calculating M_∞ from the given atmospheric pressure and density, the Mach limits of the termination region will be slightly different based on the γ for each case.

[e]Representative of the SRP jet physics shown in Figure 4.

[f]Run with the same trajectory propagation method as the other cases so that it would be subject to the same constraints; the actual Mars Pathfinder mission resulted in a trajectory passing through the middle of the termination region, while the maximum mass requirement of the cases run here allows the trajectory to pass through the edge of this envelope.

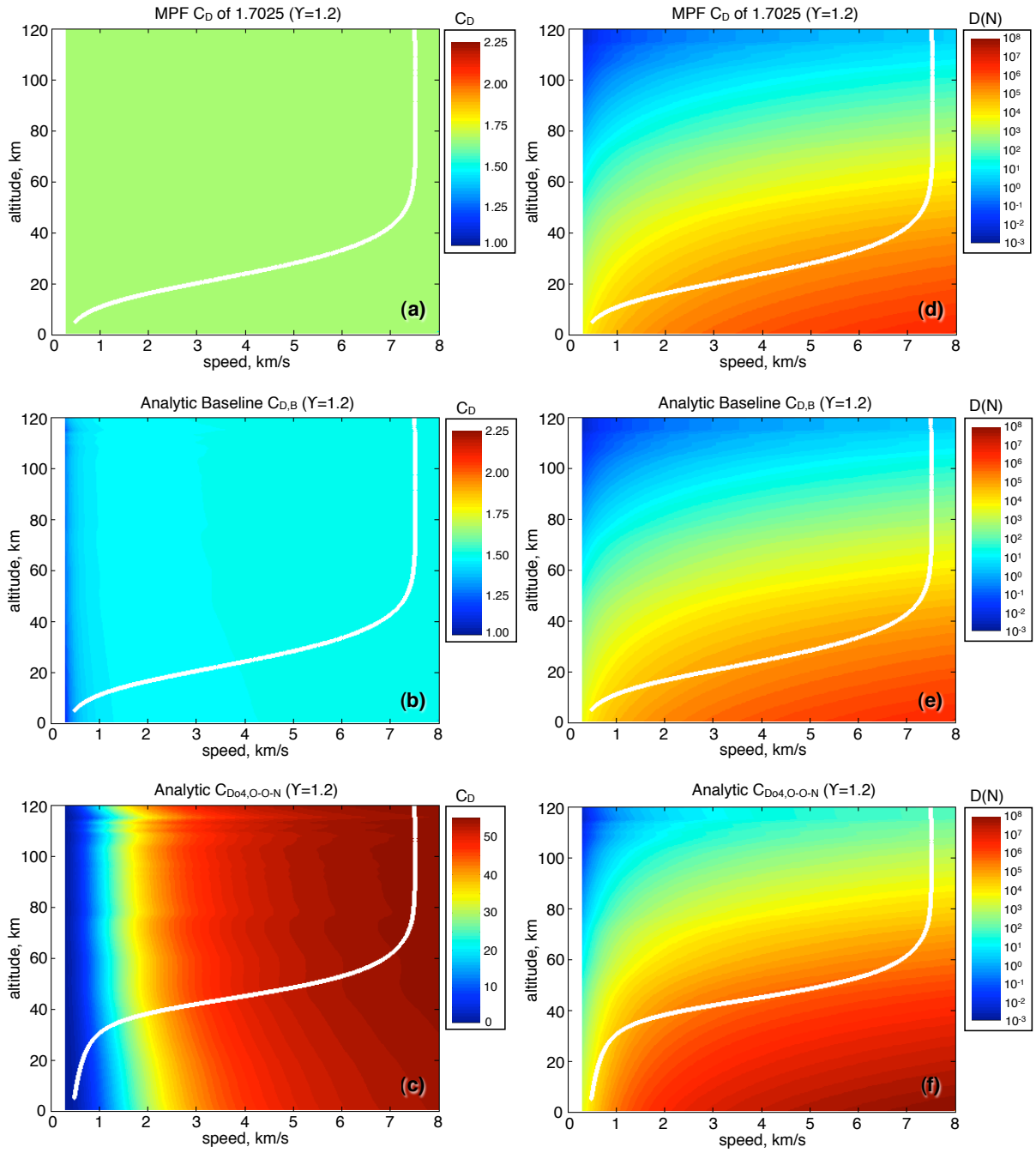

Figure 16. Maximum C_D contours (left column) and corresponding drag contours (right column) for the constant (MPF), baseline, and sample shock cascade cases. Maximum mass trajectory solutions are overlaid in white. Note that (a) and (b) use an expanded color map as compared to (c) to illustrate slight C_D differences, and that the drag maps of (d)-(f) are logarithmic.

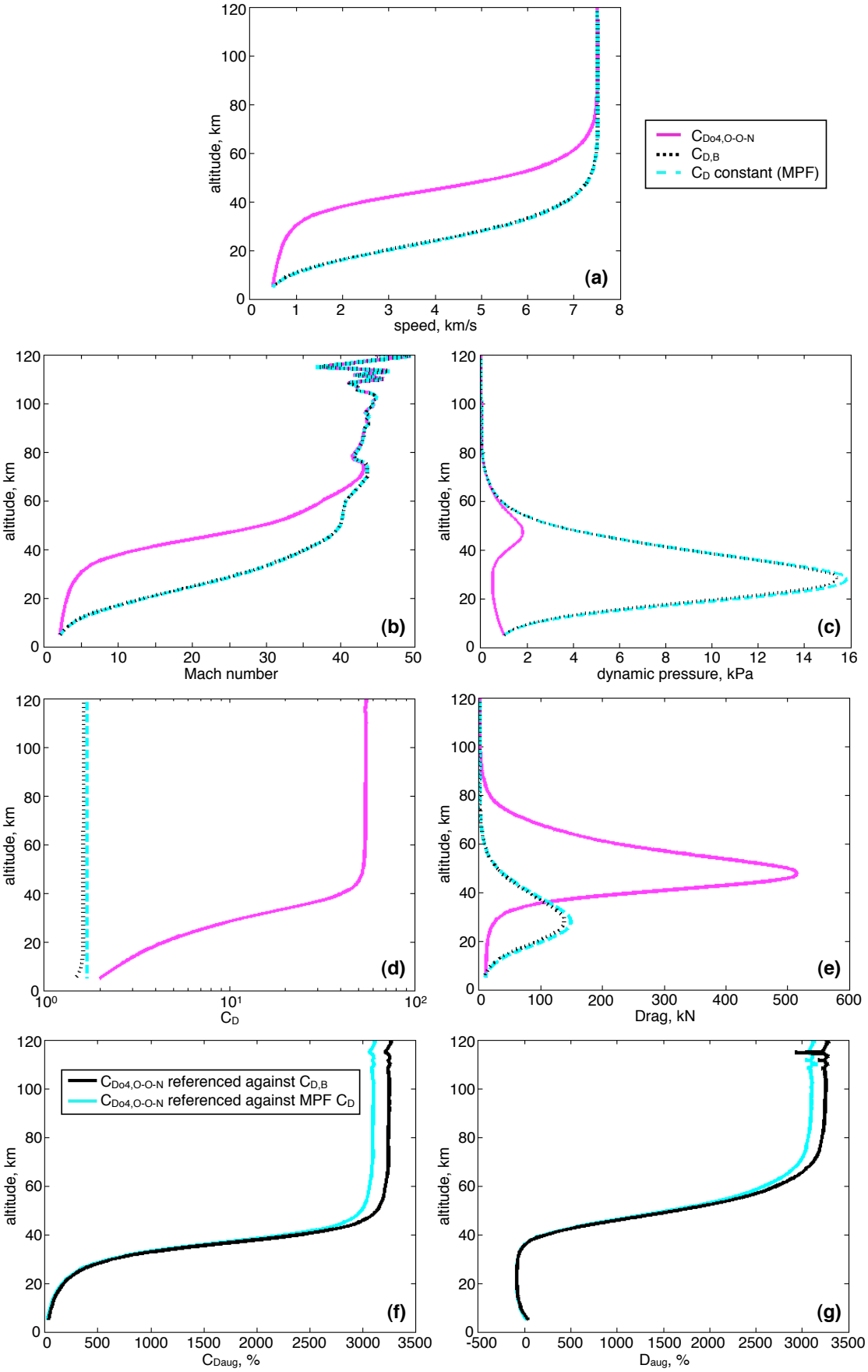

Figure 17. (a)-(e) Trajectory-specific results for the constant (MPF), baseline, and sample shock cascade cases as a function of altitude. (f)-(g) Shock cascade augmentation values as compared to the baseline and constant C_D cases.

case, these drag values extend into the high altitude-low speed regions of the space (Fig. 16f), manifested as a "red shift" of the drag map upwards and to the left. All three cases experience similar drag values at the very lowest speeds since the drag coefficients in that range are comparable. Note the drag values on the order of $10^6 N$ based on the C_D profile of this sample shock cascade, achievable through SRP-based shock manipulation.

The trajectories of each case overlay the contours of Figure 16 and can be related through the equations of motion; for constant mass, increasing drag leads to stronger vehicle deceleration. Figure 17 compares trajectory-specific characteristics for each case as a function of altitude. Comparing the trajectories of the three cases (Fig. 17a), the shock cascade case exhibits the majority of its deceleration much higher in the atmosphere ($\sim 50km$) due to the order of magnitude higher drag values in that region as compared to the baseline and constant-C_D MPF cases which reach a much lower altitude ($\sim 30km$) before experiencing enough drag for substantial deceleration. This disparity results in freestream Mach numbers of 5 being reached at approximately $30km$ altitude for the shock cascade case while the baseline case reached Mach 5 at only $10km$ (Fig. 17b). Of note is the almost linear change in velocity as the low-C_D cases drop through the atmosphere towards the termination region, whereas the shock cascade case experiences a rapid altitude loss at almost constant speed at the end of its trajectory. This is due to the choice of termination criteria in a region of both low q_∞ and low M_∞, resulting in a low C_D and drastically lower drag values. Figures 17(c,e) reveal the dynamic pressure variation over the trajectories and the subsequent drag development. C_D and drag augmentation are plotted in Figures 17(f,g) and indicate a 3000% drag increase over the baseline and MPF cases at high-altitudes due to shock manipulation via SRP.

Before examining payload mass benefits, recollect that the trajectories we considered here represent the maximum total vehicle mass (constant along the entire trajectory) capable of ending in the termination region for each case. Listed in Table 2, we see that the shock cascade case is capable of decelerating a 2.7 times larger mass than the baseline and constant-C_D cases. To gain an understanding of feasible payload mass fractions, we use a simple assumption that the infrastructure mass (defined here as the difference between total mass and payload mass) of each case is the same, since the aeroshell diameter is constant and the same DGB parachute can be utilized since each case reaches the deployment region. For this quick estimation, we don't consider the varying mass of propellant needed for supersonic or subsonic retropropulsion. With these assumptions, we can use a constant infrastructure mass of $493kg$ (based on the Mars Pathfnder mission) to determine feasible payload masses and the resulting payload mass fractions (PMF), calculated in Table 2. The shock cascade case enables a payload mass fraction of 76%, almost doubling the maximum PMF of the MPF-based constant-C_D case and resulting in almost 5 times the payload mass.

Table 2. Maximum mass and PMF estimates associated with Figs. 16 and 17.

case	total mass	$\frac{total\ mass}{baseline\ mass}$	payload mass	PMF	$\frac{payload\ mass}{baseline\ payload\ mass}$
MPF	$585kg$		$92kg$	15.7%	
baseline: $C_{D,B}$	$787kg$	1.00	$294kg$	37.4%	1.00
MPF: constant C_D	$852kg$	1.08	$359kg$	42.1%	1.22
cascade: $C_{Do4,O\text{-}O\text{-}N}$	$2120kg$	2.69	$1627kg$	76.7%	5.53
delayed SRP (15km)	$2390kg$	3.04	$1897kg$	79.4%	6.45

Further, if we reconsider Figure 17c we note that the shock cascade case, although resulting in the highest drag values, did so while experiencing very low dynamic pressure values as compared to the contrasting low-C_D cases which penetrated more deeply into the atmosphere before decelerating. This suggests a prospective new strategy - if SRP activation is delayed until the vehicle is deeper in the atmosphere, we can exploit even more of the drag potential thanks to the increase in dynamic pressure.

A single example demonstrating this strategy was performed with the vehicle entering with the baseline C_D profile (Fig. 16b) and a simulated SRP start up (switch to shock cascade C_D contours of Fig. 16c) at $15km$ altitude. Figure 18a illustrates the resulting trajectory and drag contours as compared to the cases with SRP-on (simulated here with $C_{Do4,O\text{-}O\text{-}N}$) from atmospheric entry and the baseline $C_{D,B}$ case. Drag coefficient, q_∞, and drag are shown in Figures 18(b-d), demonstrating the high dynamic pressure values achieved at SRP initiation (almost two orders of magnitude larger than the SRP-on case) and the subsequent drag values on the order of $10^7 N$ now available. For this sample case, this strategy allows a vehicle mass of

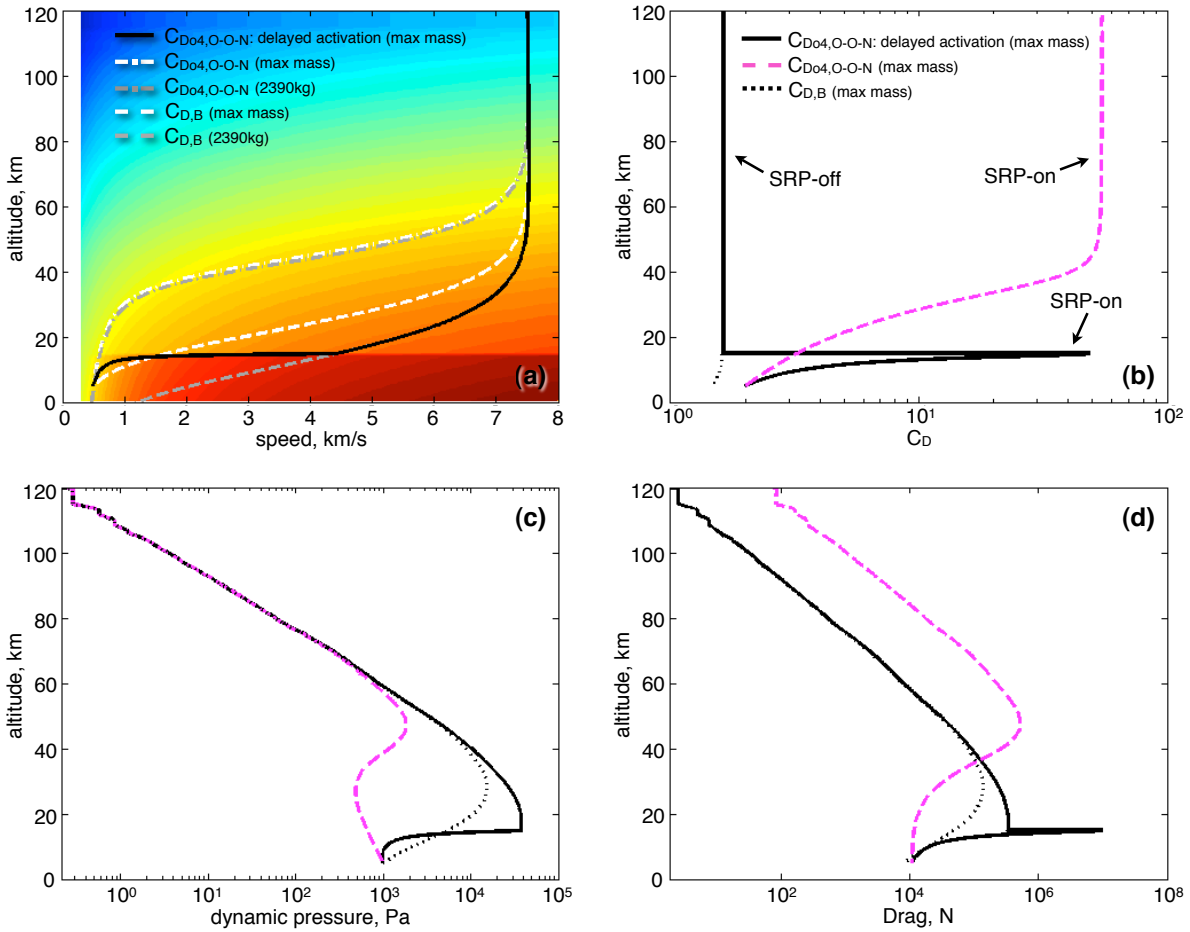

Figure 18. (a) Drag contours resulting from delayed SRP activation (at $15km$) for the O-O-N shock cascade case at γ 1.2. The resulting max-mass ($2390kg$) trajectory (black) is compared with the baseline and shock cascade max-mass trajectories (white), which decelerate at higher altitudes and experiencing less drag force. Additional comparison against baseline and shock cascade trajectories with a vehicle mass of $2390kg$ (too massive to reach termination region) are shown in gray. (b)-(d) Trajectory-specific results as a function of altitude highlighting the the significantly higher q_∞ and drag values due to delayed activation.

$2390kg$ and a PMF of almost 80%, allowing a payload mass more than 6 times larger than the baseline case and allowing $270kg$ more payload than the SRP case without delayed start up (Table 2). The strategy of delaying SRP activation will be fully explored in future work.

2. Shock Structure and γ Variation

Having determined basic trends and characteristics in the previous section, Table 3 presents maximum possible vehicle masses and estimated payload masses from trajectory computations based on each analytical C_D profile in Section IIIA. Applied C_D profiles include a constant C_D case based on the MPF value of 1.7025, the analytical baseline value representing a typical entry bow shock, analytical values ranging from a single cascade structure (O-N) to the more complex O-O-O-N cascade, and the blended cascade case assuming that the vehicle front face is affected in equal parts by flow having passed through N, O-N, and O-O-N shock structures. All 7 cases were run for γ values of 1.2, 1.3, and a sample Mars entry scenario with a 1.2 to 1.3 γ transition at Mach 5 as discussed in Section IIIA.2. Note that the individual curves in the plots of this section are based on different vehicle masses (the maximum mass for each case).

Figure 19 illustrates the effect of varying shock structures for γ 1.2. The trajectories based on $C_{D2,B}$ and constant (MPF) C_D are extremely similar and result in payload mass fractions on the order of 40%. Addition of an oblique shock significantly augments the drag coefficient and the drag, allowing the PMF

to increase above 70%. Increasing the number of oblique shocks in the cascade does result in further PMF increases, but the benefit diminishes with each additional cascade shock. As discussed in Section IIIB.1, this is due to the dwindling dynamic pressure values as the vehicle deceleration occurs at higher altitudes.

The influence of γ is demonstrated in Figure 20, with γ values of 1.2 and 1.3 compared for the baseline, O-O-O-N, and blended cascade cases. As discussed in Section IIIA.2, lower γ values result in higher analytical C_D values at all freestream Mach numbers[g]. Interestingly, this results in higher drag at high altitude, and thus γ 1.2 cases experience deceleration at the highest altitude, bleeding all q_∞ and reducing the overall vehicle mass benefits. This is highlighted in Figures 20(b-d) when comparing the two O-O-O-N (blue) curves: the γ 1.3 curve (dotted) experiences lower C_D but higher q_∞, thus the drag is comparable to the γ 1.2 case but at a slightly lower altitude. Ultimately, the γ 1.3 O-O-O-N case results in a higher possible vehicle mass as well, along with a payload mass fraction approaching 80%, due to the γ 1.2 case experiencing extremely low q_∞ and drag as it approaches the termination region from high altitudes. This trend was also seen in the O-O-N and blend cascade cases. With the delayed SRP activation strategy described in the previous section, the high-C_D potential evident in the low γ cases can be fully exploited, and these cases can result in higher mass values.

Finally, Figure 21 shows an example case (O-O-O-N) for a model Mars entry with a γ switch from 1.2 to 1.3 at Mach 5 (Section IIIA.2). As expected, this model Mars case follows the γ 1.2 curve until Mach 5 is reached, at which point the C_D and thus drag and deceleration decreases[h]. This γ switch results in the lowest vehicle mass as compared to the γ 1.2 and 1.3 cases as a consequence of experiencing both diminished q_∞ due to high-altitude deceleration (γ 1.2) and low drag coefficients at low altitudes (γ 1.3).

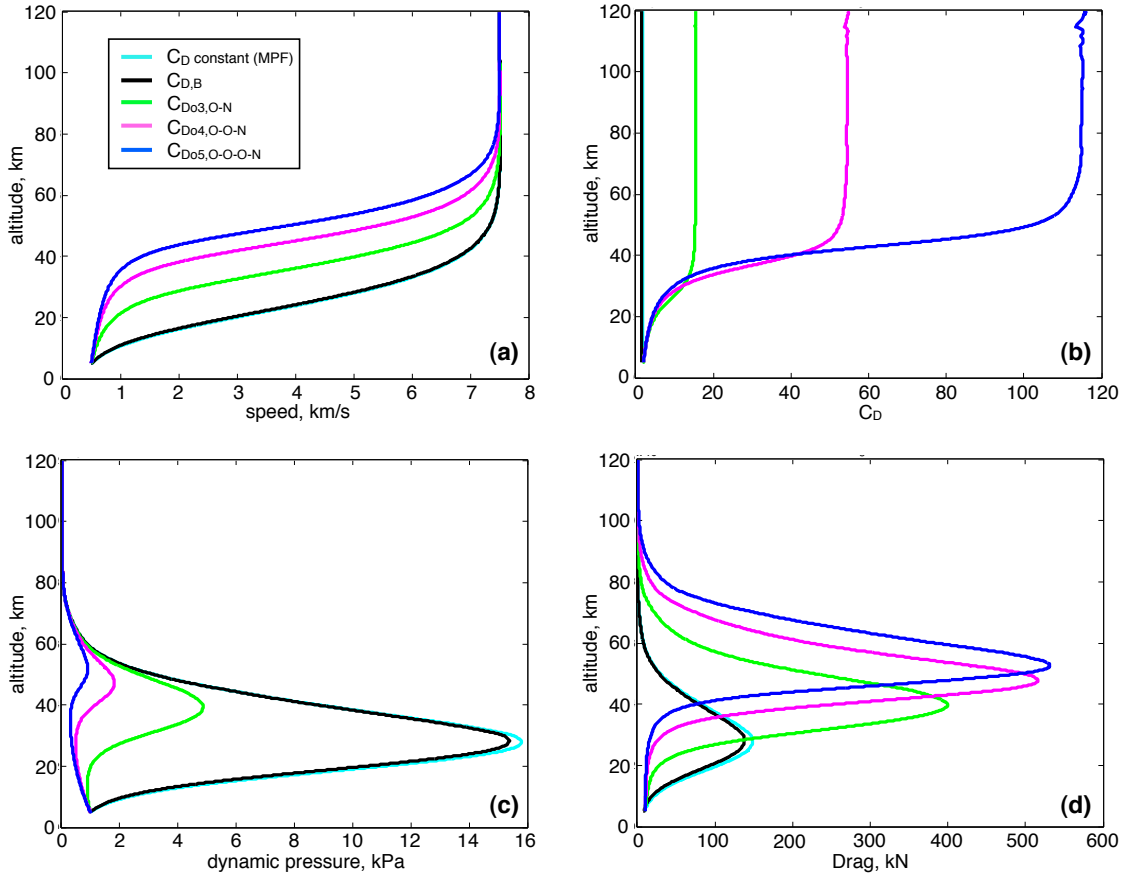

Figure 19. Trajectory-specific results as a function of altitude for each shock case, compared to the $C_{D,B}$ case.

[g]Note that Figure 20b shows C_D as a function of altitude and not Mach number.
[h]Entry into the true Martian atmosphere would result in a smoother γ transition.

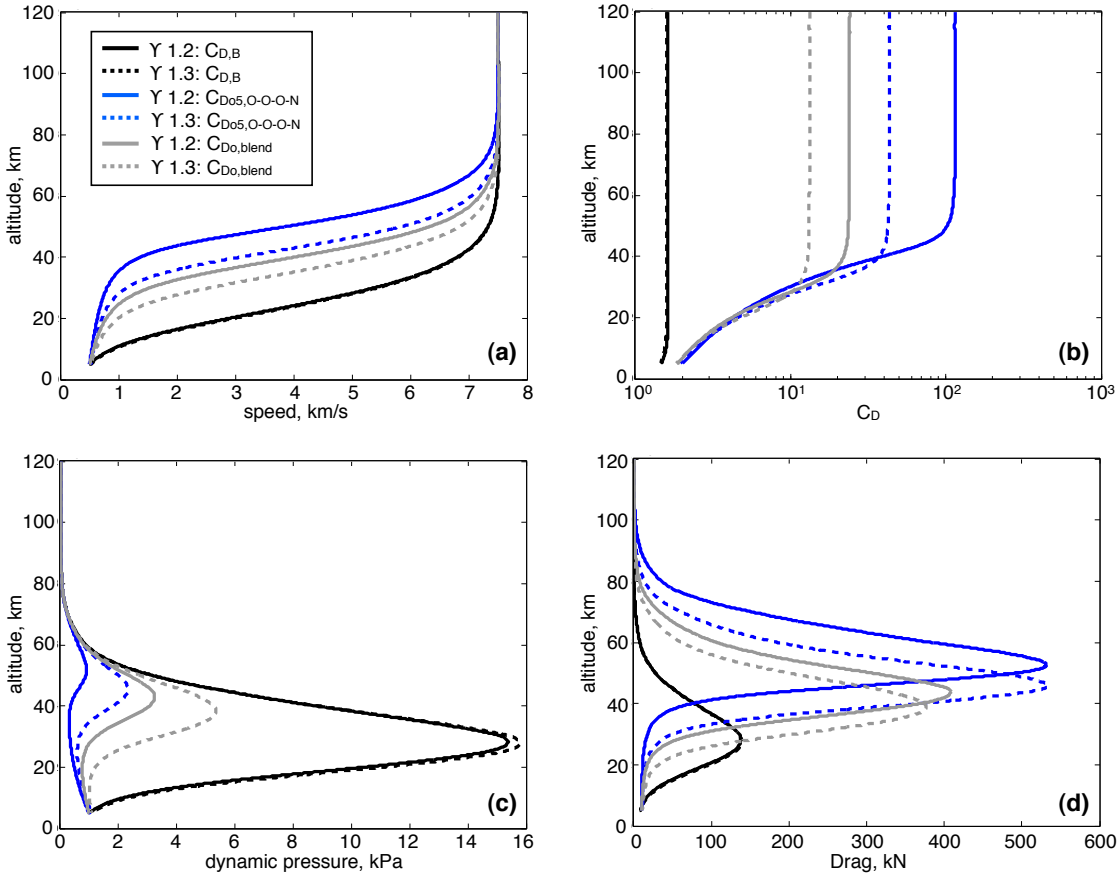

Figure 20. γ comparisons for the baseline, blend, and O-O-O-N cases.

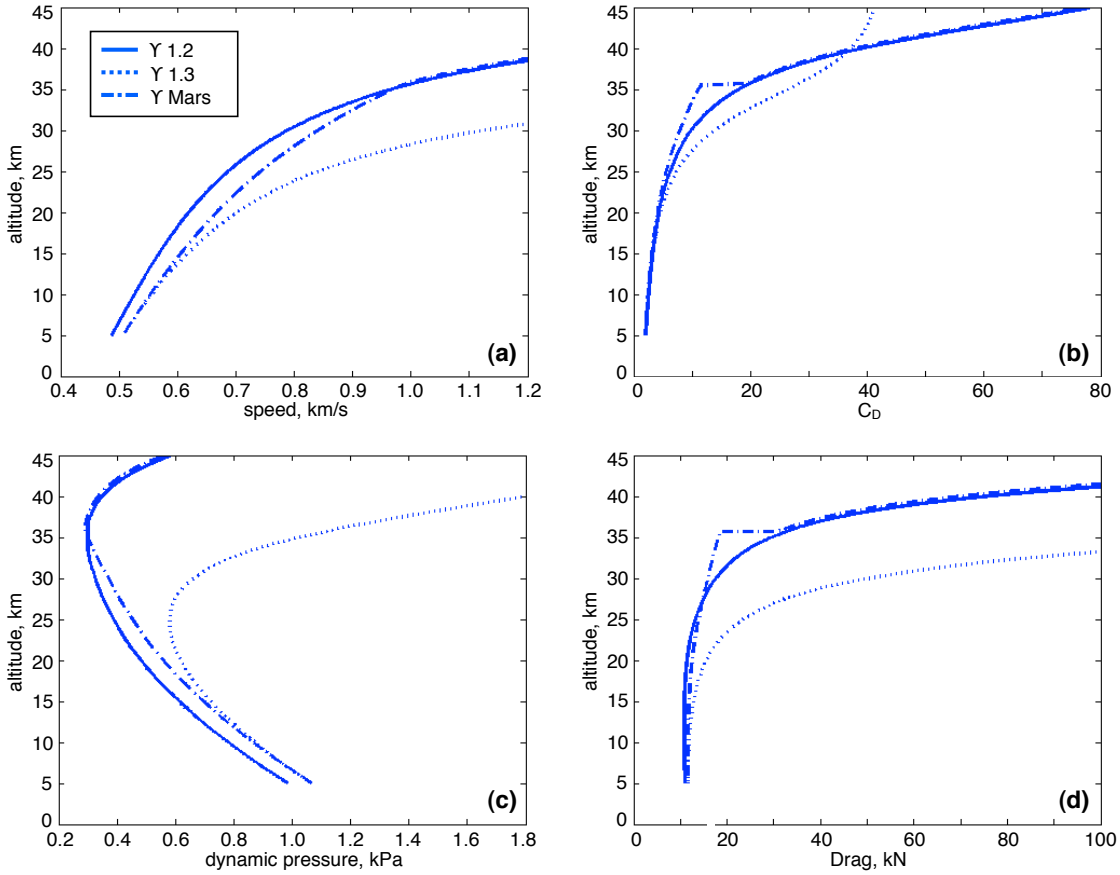

Figure 21. γ comparisons (O-O-O-N case), illustrating effects of the model Mars entry γ_{eff} switch at Mach 5.

Table 3. Maximum mass and PMF estimates for each shock structure at various γ.

γ	case	total mass	$\frac{\text{total m}}{\text{baseline m}}$	payload mass	$\frac{\text{payload m}}{\text{baseline payload m}}$	PMF
	MPF	$585kg$		$92kg$		15.7%
1.2	baseline: $C_{D,B}$	$787kg$	1.00	$294kg$	1.00	37.4%
1.2	MPF: constant C_D	$852kg$	1.08	$359kg$	1.22	42.1%
1.2	cascade: $C_{Do2,N}$	$925kg$	1.18	$432kg$	1.47	46.7%
1.2	cascade: $C_{Do3,O\text{-}N}$	$1885kg$	2.40	$1392kg$	4.73	73.8%
1.2	cascade: $C_{Do4,O\text{-}O\text{-}N}$	$2120kg$	2.69	$1627kg$	5.53	76.7%
1.2	cascade: $C_{Do5,O\text{-}O\text{-}O\text{-}N}$	$2138kg$	2.72	$1645kg$	5.60	76.9%
1.2	cascade: $C_{Do,blend}$	$1801kg$	2.29	$1308kg$	4.45	72.6%
1.3	baseline: $C_{D,B}$	$797kg$	1.00	$304kg$	1.00	38.1%
1.3	MPF: constant C_D	$879kg$	1.10	$386kg$	1.27	43.9%
1.3	cascade: $C_{Do2,N}$	$937kg$	1.18	$444kg$	1.46	47.4%
1.3	cascade: $C_{Do3,O\text{-}N}$	$1884kg$	2.36	$1391kg$	4.58	73.8%
1.3	cascade: $C_{Do4,O\text{-}O\text{-}N}$	$2180kg$	2.74	$1687kg$	5.55	77.4%
1.3	cascade: $C_{Do5,O\text{-}O\text{-}O\text{-}N}$	$2228kg$	2.80	$1735kg$	5.71	77.9%
1.3	cascade: $C_{Do,blend}$	$1813kg$	2.27	$1320kg$	4.34	72.8%
Mars	baseline: $C_{D,B}$	$804kg$	1.00	$311kg$	1.00	38.7%
Mars	MPF: constant C_D	$877kg$	1.09	$384kg$	1.23	43.8%
Mars	cascade: $C_{Do2,N}$	$945kg$	1.18	$452kg$	1.45	47.8%
Mars	cascade: $C_{Do3,O\text{-}N}$	$1891kg$	2.35	$1398kg$	4.50	73.9%
Mars	cascade: $C_{Do4,O\text{-}O\text{-}N}$	$2087kg$	2.60	$1594kg$	5.13	76.4%
Mars	cascade: $C_{Do5,O\text{-}O\text{-}O\text{-}N}$	$2079kg$	2.59	$1586kg$	5.10	76.3%
Mars	cascade: $C_{Do,blend}$	$1786kg$	2.22	$1293kg$	4.16	72.4%

C. Drag Potential

Recent SRP research has focused on increasing thrust levels to meet the deceleration requirements of upcoming large-payload Mars missions. Our study takes an alternative approach, emphasizing the potential of aerodynamic drag on the entry body. Cascading shock structures generated via modest SRP jets enable the recovery of high pressures on the capsule face, resulting in substantially augmented C_D values as discussed in Section IIIA. When magnified by q_∞, these C_D values translate into an immense drag potential as exemplified by Figure 16f. The proposed strategy of delayed SRP activation (Sec. IIIB.1) offers just one method of exploiting this untapped reservoir of potential drag. We now quantify the maximum drag potential of various shock structures to determine the feasibility of SRP-based drag augmentation as a competitive EDL technology.

Drag potential, the absolute upper limit on achievable drag in a given altitude-velocity space, is estimated based on a max-q_∞[i] value and the maximum C_D value[j] associated with each shock structure. Figure 22 displays these drag/S_{ref} values[k] as a function of achieved percentage of the potential drag value, revealing the benefits of this drag augmentation method even for sub-optimal trajectories subject to constraints.

In comparison with the analytical maximum drag/S_{MPF} value of the (SRP-off) Mars Pathfinder trajectory, $2.7\text{x}10^4 N/m^2$ (dotted black line), a simple O-N shock structure with delayed SRP activation has the potential to reach drag values of $3.7\text{x}10^6 N/m^2$, and more substantial cascades such as O-O-O-N are capable of achieving drag values of $2.8\text{x}10^7 N/m^2$, more than a 3-order of magnitude increase representing a huge decelerative capacity. Note that the solid lines in the figure represent the most extreme SRP activation delay, so the MPF-based C_D value (cyan line) based on this activation strategy gains an order of magnitude in drag potential as compared to the established MPF trajectory. However, shock manipulation leading to

[i]Evaluated using a minimum altitude requirement of $5km$ and maximum velocity of $7500m/s$ based on the trajectory study of Section IIIB.

[j]From the limiting C_D value at γ 1.2 as reported in Table 6.

[k]Independent of entry vehicle sizing (S_{ref}).

shock cascades still provides drag benefits on the order of 10 to 100 times increase.

For example, Figure 23 superimposes the O-O-N drag map of Figure 16f with contour lines showing the achieved percentage of the maximum potential drag for that shock structure. The maximum mass trajectory for the analytical O-O-N case (solid white line), which achieved a payload mass increase of more than 5.5 times over the baseline value, reaches less than 1% of the potential drag value. This small but significant drag augmentation as compared to the SRP-off case (Fig. 22) is consistent with the drag differences observed in Figure 18d. Delaying SRP activation until $15km$ altitude (dashed white line in Fig. 23) produces drag on the order of more than 10% of the maximum possible drag value, a significant drag augmentation over the SRP-off case as compared in Figures 22 and 18d, illustrating the potential of this strategy for tapping into the drag reservoir produced through shock manipulation.

Finally, as compared to recent system-level SRP studies[4,34,48] expressing an upper bound on available SRP thrust force[l] of the order $T_{max}/S_{ref} \approx 1.3\mathbf{x}10^5 N/m^2$, even conservative SRP-based drag estimates provide an order of magnitude force augmentation, establishing the potential of this concept for Mars EDL systems.

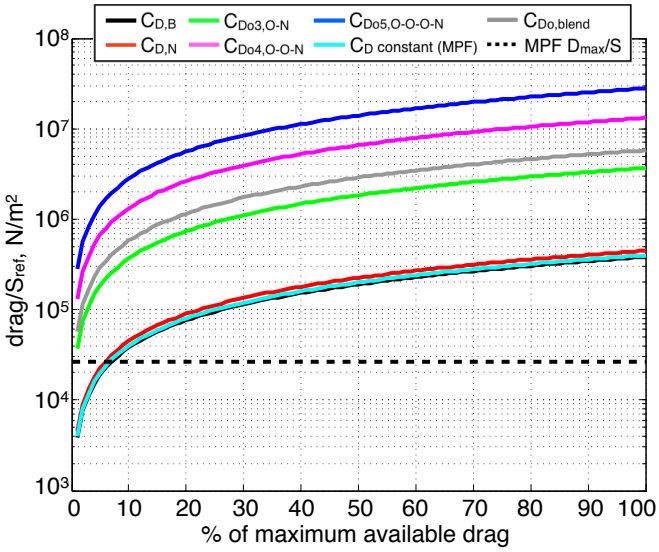

Figure 22. Drag per reference area as a function of achieved % of maximum drag for each shock structure (100% is the potential drag value). The dotted black line represents the maximum drag value attained over the analytical (SRP-off) Mars Pathfinder trajectory.

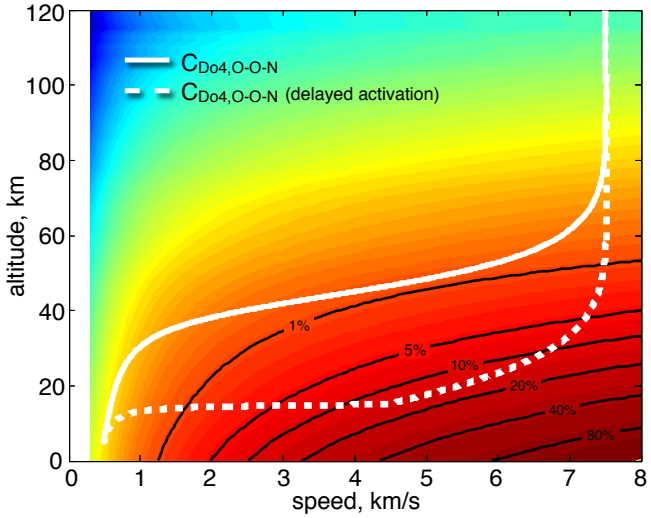

Figure 23. O-O-N drag map (γ 1.2) superimposed with black contour lines showing achieved % of potential drag for that shock structure. Overlays of the maximum mass trajectories for O-O-N (SRP-on over entire trajectory) and delayed activation O-O-N are also portrayed. Note the drag map does not apply to the delayed activation trajectory at altitudes higher than $15km$.

[l]Based on maximum thrust values of $10^6 N$ and a $10m$ diameter vehicle (conservative baed on the ranges given in Refs. 34 and 48).

IV. Conclusion

The use of high-thrust supersonic retropropulsion systems has been proposed as a candidate enabling technology for future high-mass Mars missions. Rather than rely solely on this paradigm of thrust escalation, the current study examined the potential for aerodynamic drag augmentation via modestly powered SRP systems, offering the potential for significant deceleration without the burden of increased fuel mass. Rooted in the idea that stagnation pressure represents an available reservoir of potential drag, we studied the benefit of shock manipulation via SRP jets to exploit the high energies inherent in entry scenarios.

An analytical study was performed to quantify the maximum drag coefficients attainable based on various shock structures, demonstrating the ability to generate C_D values on the order of 50 for simple cascades. A trajectory propagation method enabled calculation of drag and maximum landed mass for each C_D profile, revealing tremendous increases in aerodynamic drag starting at approximately $60km$ above the surface. The significant drag augmentation observed in some cases allowed for estimated payload mass fractions approaching 78%. In addition, examining the effect of specific heat ratio (γ) illustrated the heavy dependence of C_D on γ, with the low γ values typical in Mars entry scenarios further increasing C_D levels. Finally, we identified a strategy of delayed SRP activation in order to wield substantially higher q_∞, resulting in potential drag values (per reference area) on the order of $10^7 N/m^2$, an orders of magnitude increase over typical entry values. The drag potential achievable through SRP-based flow control demonstrates the capability of this nascent concept to satisfy the decelerative needs of high-mass Mars entry scenarios.

With the maximum drag limits for a range of shock structures identified, detailed SRP simulations are planned to establish attainable C_D values through manipulation of the bow shock system with relatively low thrust SRP jets. In addition, follow-on trajectory studies exploiting the optimal drag potential subject to heating and acceleration constraints will result in subsequent estimates of realizable drag and achievable payload mass for flow-control SRP systems.

Acknowledgments

N. Bakhtian thanks the Stanford Graduate Fellowship Program, Zonta International Amelia Earhart Fellowship Program, and NASA Education Associates Program for financial support. We would like to thank Jim Weilmuenster, Ken Sutton, and Peter Gnoffo at NASA Langley for their atmospheric entry expertise, Loc Huynh and Jeffrey Bowles at NASA Ames for their assistance with trajectory propagation, and Juan Alonso (Stanford University), Marian Nemec (NASA Ames), Seokkwan Yoon (NASA Ames), Ashley Korzun (Georgia Institute of Technology), Karl Edquist (NASA Langley), and Thomas Pulliam (NASA Ames) for many useful discussions. We also gratefully acknowledge the support of the NASA Advanced Supercomputing Division for access to the Columbia and Pleiades superclusters upon which these studies were performed.

References

[1]Manning, R. M. and Adler, M., "Landing on Mars," AIAA Paper 2005-6742, AIAA SPACE 2005 Conference & Exposition, Long Beach, CA, September 2005.

[2]Braun, R. D. and Manning, R. M., "Mars Exploration Entry, Descent, and Landing Challenges," *Journal of Spacecraft and Rockets*, Vol. 44, No. 2, March-April 2007, pp. 310–323.

[3]Drake, B. G. (Editor), "Human Exploration of Mars, Design Reference Architecture 5.0," NASA SP-2009-566, Mars Architecture Steering Group, NASA Headquarters, July 2009.

[4]Edquist, K. T., Dyakonov, A. A., Korzun, A. M., Shidner, J. D., Studak, J. W., Tigges, M. A., Kipp, D. M., Prakash, R., Trumble, K. A., and Dupzyk, I. C., "Development of Supersonic Retro-Propulsion for Future Mars Entry, Descent, and Landing Systems," AIAA Paper 2010-5046, AIAA/ASME Joint Thermophysics and Heat Transfer Conference, Chicago, IL, July 2010.

[5]Hayman, L. O. and McDearmon, Jr., R. W., "Jet Effects on Cylindrical Afterbodies Housing Sonic and Supersonic Nozzles Which Exhaust Against a Supersonic Stream at Angles of Attack from 90° to 180°," NASA Technical Note NASA-TN-D-1016, Langley Research Center, Langley Air Force Base, VA, March 1962.

[6]Peterson, V. L. and McKenzie, R. L., "Effects of Simulated Retrorockets on the Aerodynamic Characteristics of a Body of Revolution at Mach Numbers from 0.25 to 1.90," NASA Technical Note D-1300, Ames Research Center, Moffett Field, CA, May 1962.

[7]Keyes, J. W. and Hefner, J. N., "Effect of Forward-Facing Jets on Aerodynamic Characteristics of Blunt Configurations at Mach 6," *Journal of Spacecraft*, Vol. 4, No. 4, April 1967, pp. 533–534.

[8]Jarvinen, P. O. and Adams, R. H., "The Effects of Retrorockets on the Aerodynamic Characteristics of Conical Aeroshell Planetary Entry Vehicles," AIAA Paper 70-219, AIAA 8th Aerospace Sciences Meeting, New York, NY, January 1970.

[9]Grenich, A. F. and Woods, W. C., "Flow Field Investigation of Atmospheric Braking for High Drag Vehicles with Forward Facing Jets," AIAA Paper 1981-0293, 19th AIAA Aerospace Sciences Meeting, St. Louis, MO, January 1981.

[10]Drake, B. G. (Editor), "Reference Mission Version 3.0, Addendum to the Human Exploration of Mars: The Reference Mission of the NASA Mars Exploration Study Team," NASA SP-6107-ADD, Exploration Office, NASA Johnson Space Center, June 1998.

[11]Drake, B. G. (Editor), "Human Exploration of Mars, Design Reference Architecture 5.0: Addendum," NASA SP-2009-566-ADD, Mars Architecture Steering Group, NASA Headquarters, July 2009.

[12]Zang, T. A. (Editor), "Entry, Descent and Landing Systems Analysis Study: Phase 1 Report," NASA TM-2010-216720, EDL Systems Analysis Team, May 2010.

[13]Berry, S. A., Laws, C. T., Kleb, W. L., Rhode, M. N., Spells, C., Mccrea, A. C., Trumble, K. A., Schauerhamer, D. G., and Oberkampf, W. L., "Supersonic Retro-Propulsion Experimental Design for Computational Fluid Dynamics Model Validation," IEEEAC 1499, IEEE Aerospace Conference, Big Sky, MT, March 2011.

[14]Alkandry, H., Boyd, I. D., Reed, E. M., Codoni, J. R., and McDaniel, J. S., "Interactions of Single-Nozzle Sonic Propulsive Deceleration Jets on Mars Entry Aeroshells," AIAA Paper 2010-4888, AIAA/ASME Joint Thermophysics and Heat Transfer Conference, Chicago, IL, July 2010.

[15]Codoni, J. R., Reed, E. M., McDaniel, J. S., Alkandry, H., and Boyd, I. D., "Investigations of Peripheral 4-jet Sonic and Supersonic Propulsive Deceleration Jets on a Mars Science Laboratory Aeroshell," AIAA Paper 2011-1036, 49th AIAA Aerospace Sciences Meeting, Orlando, FL, January 2011.

[16]Alkandry, H., Boyd, I. D., Reed, E. M., Codoni, J. R., and McDaniel, J. S., "Interactions of Single-Nozzle Supersonic Propulsive Deceleration Jets on Mars Entry Aeroshells," AIAA Paper 2011-138, 49th AIAA Aerospace Sciences Meeting, Orlando, FL, January 2011.

[17]Bakhtian, N. M. and Aftosmis, M. J., "Parametric Study of Peripheral Nozzle Configurations for Supersonic Retropropulsion," AIAA Paper 2010-1239, 48th AIAA Aerospace Sciences Meeting, Orlando, FL, January 2010.

[18]Korzun, A. M., Cordell, C. E., and Braun, R. D., "Comparison of Inviscid and Viscous Aerodynamic Predictions of Supersonic Retropropulsion Flowfields," AIAA Paper 2010-5048, AIAA/ASME Joint Thermophysics and Heat Transfer Conference, Chicago, IL, July 2010.

[19]Trumble, K. A., Schauerhamer, D. G., Kleb, W. L., Carlson, J.-R., Buning, P. G., Edquist, K., and Barnhardt, M. D., "An Initial Assessment of Navier-Stokes Codes Applied to Supersonic Retro-Propulsion," AIAA Paper 2010-5047, AIAA/ASME Joint Thermophysics and Heat Transfer Conference, Chicago, IL, July 2010.

[20]Schauerhamer, D. G., "Ongoing Study of Supersonic Retro-Propulsion Using Structured Overset Grids and OVERFLOW," Presentation, 10th Symposium on Overset Composite Grids and Solution Technology, Moffett Field, CA, September 2010.

[21]Trumble, K. A., Schauerhamer, D. G., Kleb, W. L., Carlson, J.-R., and Edquist, K. T., "Analysis of Navier-Stokes Codes Applied to Supersonic Retro-Propulsion Wind Tunnel Test," IEEEAC 1471, IEEE Aerospace Conference, Big Sky, MT, March 2011.

[22]Cordell, C. E., Clark, I. G., and Braun, R. D., "CFD Verification of Supersonic Retropropulsion for a Central and Peripheral Configuration," IEEEAC 1190, IEEE Aerospace Conference, Big Sky, MT, March 2011.

[23]Schauerhamer, D. G., Trumble, K. A., Kleb, W. L., Carlson, J.-R., Buning, P. G., Edquist, K. T., and Sozer, E., "Ongoing Validation of Computational Fluid Dynamics for Supersonic Retro-Propulsion," Paper, 8th International Planetary Probe Workshop, Portsmouth, VA, June 2011.

[24]Jarvinen, P. O. and Adams, R. H., "The Aerodynamic Characteristics of Large Angled Cones with Retrorockets," NASA Contract No. NAS7-576, Cambridge, MA, Feb. 1970.

[25]Daso, E. O., Pritchett, V. E., Wang, T.-S., Ota, D. K., Blankson, I. M., and Auslender, A. H., "The Dynamics of Shock Dispersion and Interactions in Supersonic Freestreams with Counterflowing Jets," AIAA Paper 2007-1423, 45th AIAA Aerospace Sciences Meeting, Reno, NV, January 2007.

[26]Daso, E. O., Pritchett, V. E., Wang, T.-S., Ota, D. K., Blankson, I. M., and Auslender, A. H., "Dynamics of Shock Dispersion and Interactions in Supersonic Freestreams with Counterflowing Jets," *AIAA Journal*, Vol. 47, No. 6, June 2009, pp. 1313–1326.

[27]Bakhtian, N. M. and Aftosmis, M. J., "Parametric Study of Peripheral Nozzle Configurations for Supersonic Retropropulsion," *Journal of Spacecraft and Rockets*, Vol. 47, No. 6, November-December 2010, pp. 935–950.

[28]Korzun, A. M., Cruz, J. R., and Braun, R. D., "A Survey of Supersonic Retropropulsion Technology for Mars Entry, Descent, and Landing," *Journal of Spacecraft and Rockets*, Vol. 46, No. 5, September-October 2009, pp. 929–937.

[29]Menezes, V., Saravanan, S., Jagadeesh, G., and Reddy, K. P. J., "Experimental Investigations of Hypersonic Flow over Highly Blunted Cones with Aerospikes," *AIAA Journal*, Vol. 41, No. 10, October 2003, pp. 1955–1966.

[30]Wells, G., Lafleur, J., Verges, A., Manyapu, K., Christian, J. A., Lewis, C., and Braun, R. D., "Entry, Descent, and Landing Challenges of Human Mars Exploration," AAS 06-072, 29th Annual AAS Guidance and Control Conference, Breckenridge, CO, February 2006.

[31]Christian, J. A., Wells, G., Lafleur, J., Verges, A., and Braun, R. D., "Extension of Traditional Entry, Descent, and Landing Technologies for Human Mars Exploration," *Journal of Spacecraft and Rockets*, Vol. 45, No. 1, January-February 2008, pp. 130–141.

[32]Cianciolo, A. D., Davis, J. L., Shidner, J. D., and Powell, R. W., "Entry, Descent and Landing Systems Analysis: Exploration Class Simulation Overview and Results," AIAA Paper 2010-7970, AIAA/AAS Astrodynamics Specialist Conference, Toronto, ON, August 2010.

[33]Zang, T. A., Dwyer-Cianciolo, A. M., Kinney, D. J., Howard, A. R., Chen, G. T., Ivanov, M. C., Sostaric, R. R., and Westhelle, C. H., "Overview of the NASA Entry, Descent and Landing Systems Analysis Study," AIAA Paper 2010-8649, AIAA SPACE 2010 Conference & Exposition, Anaheim, CA, September 2010.

[34]Korzun, A. M. and Braun, R. D., "Performance Characterization of Supersonic Retropropulsion for Application to High-Mass Mars Entry, Descent, and Landing," AIAA Paper 2009-5613, AIAA Atmospheric Flight Mechanics Conference, Chicago, IL, August 2009.

[35]Korzun, A. M. and Braun, R. D., "Performance Characterization of Supersonic Retropropulsion for High-Mass Mars Entry Systems," *Journal of Spacecraft and Rockets*, Vol. 47, No. 5, September-October 2010, pp. 836–848.

[36]Steinfeldt, B. A., Theisinger, J. E., Korzun, A. M., Clark, I. G., Grant, M. J., and Braun, R. D., "High Mass Mars Entry, Descent, and Landing Architecture Assessment," AIAA Paper 2009-6684, AIAA SPACE 2009 Conference & Exposition, Pasadena, CA, September 2009.

[37]Marsh, C. L. and Braun, R. D., "Fully-Propulsive Mars Atmospheric Transit Strategies for High-Mass Missions," *Journal of Spacecraft and Rockets*, Vol. 48, No. 2, March-April 2011, pp. 271–282.

[38]Shidner, J. D., Davis, J. L., Cianciolo, A. D., Samareh, J. A., and Powell, R. W., "Large Mass, Entry, Descent and Landing Sensitivity Results for Environmental, Performance, and Design Parameters," AIAA Paper 2010-7973, AIAA/AAS Astrodynamics Specialist Conference, Toronto, ON, August 2010.

[39]Howard, A., Stanley, D., and Williams-Byrd, J., "Mars Exploration Entry and Descent and Landing Technology Assessment Figures of Merit," AIAA Paper 2010-8676, AIAA SPACE 2010 Conference & Exposition, Anaheim, CA, September 2010.

[40]Hoerner, S. F., *Fluid-Dynamic Drag; Practical Information on Aerodynamic Drag and Hydrodynamic Resistance*, Hoerner Fluid Dynamics, 2nd ed., 1965.

[41]Aftosmis, M. J., Berger, M. J., and Melton, J. E., "Robust and Efficient Cartesian Mesh Generation for Component-Based Geometry," *AIAA Journal*, Vol. 36, No. 6, 1998, pp. 952–960.

[42]Aftosmis, M. J., Berger, M. J., and Adomavicius, G., "A Parallel Multilevel Method for Adaptively Refined Cartesian Grids with Embedded Boundaries," AIAA Paper 2000-0808, 38th AIAA Aerospace Sciences Meeting, Reno, NV, January 2000.

[43]Nemec, M. and Aftosmis, M. J., "Adjoint Error Estimation and Adaptive Refinement for Embedded-Boundary Cartesian Meshes," AIAA Paper 2007-4187, 18th AIAA Computational Fluid Dynamics Conference, Miami, FL, June 2007.

[44]Nemec, M. and Aftosmis, M. J., "Adjoint Sensitivity Computations for an Embedded-Boundary Cartesian Mesh Method," *Journal of Computational Physics*, Vol. 227, 2008, pp. 2724–2742.

[45]Nemec, M., Aftosmis, M. J., and Wintzer, M., "Adjoint-Based Adaptive Mesh Refinement for Complex Geometries," AIAA Paper 2008-0725, 46th AIAA Aerospace Sciences Meeting, Reno, NV, January 2008.

[46]Anderson, J. D., *Modern Compressible Flow with Historical Perspective*, McGraw Hill, 3rd ed., 2003.

[47]Spencer, D. A., Blanchard, R. C., Braun, R. D., Kallemeyn, P. H., and Thurman, S. W., "Mars Pathfinder Entry, Descent, and Landing Reconstruction," *Journal of Spacecraft and Rockets*, Vol. 36, No. 3, May-June 1999, pp. 357–366.

[48]Christian, J. A., Wells, G., Lafleur, J., Manyapu, K., Verges, A., Lewis, C., and Braun, R. D., "Sizing of an Entry, Descent, and Landing System for Human Mars Exploration," AIAA Paper 2006-7427, AIAA SPACE 2006 Conference & Exposition, San Jose, CA, September 2006.

[49]Vinh, N. X., Buseman, A., and Culp, R. D., *Hypersonic and Planetary Entry Flight Mechanics*, The University of Michigan Press, Ann Arbor, MI, 1980.

[50]Prince, J. L., Desai, P. N., Queen, E. M., and Grover, M. R., "Mars Phoenix Entry, Descent, and Landing Simulation Design and Modeling Analysis," AIAA Paper 2008-7507, AIAA/AAS Astrodynamics Specialist Conference, Honolulu, HI, August 2008.

[51]Dormand, J. R. and Prince, P. J., "A Family of Embedded Runge-Kutta Formulae," *Journal of Computational and Applied Mathematics*, Vol. 6, No. 1, 1980, pp. 19–26.

[52]Christian, J. A., Verges, A. M., and Braun, R. D., "Statistical Reconstruction of Mars Entry, Descent, and Landing Trajectories and Atmospheric Profiles," AIAA Paper 2007-6192, AIAA SPACE 2007 Conference & Exposition, Long Beach, CA, September 2007.

[53]Ames Research Staff, "Equations, Tables, and Charts for Compressible Flow," NACA TR-1135, 1953.

[54]Anderson, J. D., *Hypersonic and High-Temperature Gas Dynamics*, American Institute of Aeronautics and Astronautics, 2nd ed., 2006.

[55]Sutton, K., private communication, NASA Langley Research Center, Hampton, VA, March 2011.

Appendix A: Trajectory Propagation Method and Validation

In order to establish the possible landed mass benefits of the projected C_D augmentation, the entry vehicle's trajectory must be determined since the decelerating drag force is a function of both altitude and velocity: $D = \mathcal{F}(q_\infty) = \mathcal{F}(\rho_\infty, V_\infty)$. In the coming sections, we utilize a 3-DOF trajectory model[m] consisting of three kinematic equations of motion (Eqns. 30-32) and three force equations (Eqns. 33-35) as derived in Ref. 49 to propagate a set of vehicle entry conditions to the ground using a 4th-order Runge-Kutta integration method[n]. The tabulated atmospheric model, used in previous systems-level SRP studies[35,36] is based on the reconstructed Mars Pathfinder entry data of Ref. 47. Planetary constants are given in Table 4, and the gravity model is simply $g = \frac{\mu}{r_{Mars}^2}$. Force tangential to the velocity is $F_t = -D$, and, assuming no lift, the force normal to the velocity is $F_n = L = 0$.

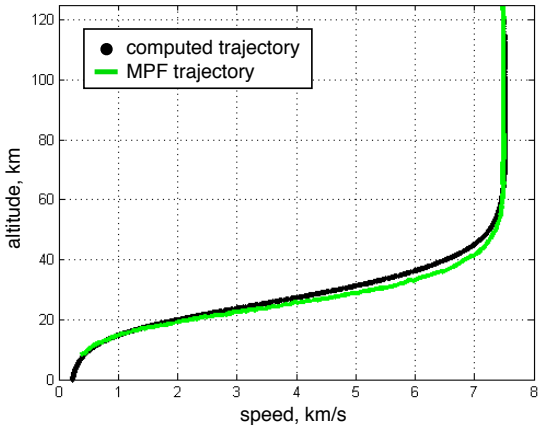

Figure 24. Comparison of computed trajectory to actual Mars Pathfinder trajectory from Ref. 50.

$$\frac{dr}{dt} = V \sin\Gamma \tag{30}$$

$$\frac{d\zeta}{dt} = \frac{V \cos\Gamma \cos\psi}{r \cos\phi} \tag{31}$$

$$\frac{d\phi}{dt} = \frac{V \cos\Gamma \sin\psi}{r} \tag{32}$$

$$\frac{dV}{dt} = \frac{F_t}{m} - g \sin\Gamma + r\omega^2 \cos\phi(\sin\Gamma \cos\phi - \cos\Gamma \sin\phi \sin\psi) \tag{33}$$

$$V\frac{d\Gamma}{dt} = \frac{F_n \cos\epsilon}{m} - g\cos\Gamma + \frac{V^2 \cos\Gamma}{r} + 2\omega V \cos\phi cos\psi + r\omega^2 \cos\phi(\cos\Gamma \cos\phi + \sin\Gamma \sin\phi \sin\psi) \tag{34}$$

$$V\frac{d\psi}{dt} = \frac{F_n \sin\epsilon}{m\cos\Gamma} - \frac{V^2 \cos\Gamma \cos\psi \tan\phi}{r} + 2\omega V(\tan\Gamma \cos\phi \sin\psi - \sin\phi) - \frac{r\omega^2 \sin\phi \cos\phi \cos\psi}{\cos\Gamma} \tag{35}$$

Table 4. Mars planetary constants.

planetary angular rotation rate	ω	$7.0882\text{x}10^{-5} rad/s$
planetary radius	r_{Mars}	$3389.5\text{x}10^{3} m$
standard gravitational parameter	μ	$4.28284\text{x}10^{13} m^3/s^2$

Validation of the 3-DOF trajectory code was performed against the Mars Pathfinder mission trajectory. Table 5 gives the initial conditions used in the propagation code, and Figure 24 shows the resulting trajectory comparison. For this validation case, C_D was assumed constant at 1.7025 (from a ballistic coefficient of 62.3), mass was assumed constant at 585kg, and reference area was based on MPF's circular aeroshell (diameter of 2.65m).

Table 5. Initial conditions for trajectory study (Ref. 52).

distance from planet center	r	$120000m + r_{Mars}$
longitude	ζ	337.9976°
latitude	ϕ	22.6303°
velocity relative to planet	V	$7500 m/s$
flight path angle	Γ	−14.06°
heading angle	ψ	196.8519°

[m] Assuming motion of a point mass around a spherical, rotating planet.
[n] *ode45()* in MATLAB implementing the RK5(4) Dormand-Prince formula.[51]

Appendix B: Shock Equations

The normal and oblique shock equations[53] used to derive Equations 17-25 are listed here for quick reference.

A. Normal Shock Equations

$$M_2^2 = \frac{1 + \frac{\gamma-1}{2} M_1^2}{\gamma M_1^2 - \frac{\gamma-1}{2}} \tag{36}$$

$$\frac{P_2}{P_1} = 1 + \frac{2\gamma}{\gamma+1}(M_1^2 - 1) \tag{37}$$

$$\frac{P_{o2}}{P_{o1}} = \frac{P_{o2}}{P_2}\frac{P_2}{P_1}\frac{P_1}{P_{o1}} \tag{38}$$

B. Oblique Shock Equations

$$M_2 = \frac{M_{n2}}{\sin(\beta - \theta)} \tag{39}$$

$$\frac{P_2}{P_1} = 1 + \frac{2\gamma}{\gamma+1}(M_{n1}^2 - 1) \tag{40}$$

$$\frac{P_{o2}}{P_{o1}} = \frac{P_{o2}}{P_2}\frac{P_2}{P_1}\frac{P_1}{P_{o1}} \tag{41}$$

where

$$M_{n1} = M_1 \sin\beta \tag{42}$$

$$M_{n2}^2 = \frac{1 + \frac{\gamma-1}{2} M_{n1}^2}{\gamma M_{n1}^2 - \frac{\gamma-1}{2}} \tag{43}$$

$$\tan\theta = 2\cot\beta \frac{M_{n1}^2 - 1}{2 + M_1^2\big(\gamma + \cos(2\beta)\big)} \tag{44}$$

Appendix C: Tabulated C_D and C_{Daug} Results

Table 6. Maximum C_D and corresponding C_{Daug} values at γ 1.4, 1.3, and 1.2.

γ	$\mathbf{C_D}$ and $\mathbf{C_{Daug}}$	$\mathbf{M_\infty = 2}$	$\mathbf{M_\infty = 5}$	$\mathbf{M_\infty = 10}$	$\mathbf{M_\infty = \infty}$
1.4	$C_{Do,B}$	1.41	1.54	1.56	1.57
	C_{Do1}	2.44	30.18	606.26	∞
	$C_{Do2,N}$	1.66	1.81	1.83	1.84
	$C_{Do3,O\text{-}N}$	1.72	4.91	7.11	8.40
	$C_{Do4,O\text{-}O\text{-}N}$	1.73	7.70	13.52	17.37
	$C_{Do5,O\text{-}O\text{-}O\text{-}N}$	1.73	9.11	17.63	23.67
	$C_{Do,blend}$	1.70	4.81	7.49	9.20
	$C_{Daug,isentropic}$	73%	1860%	38793%	∞
	$C_{Daug,N}$	18%	18%	18%	18%
	$C_{Daug,O\text{-}N}$	22%	219%	356%	436%
	$C_{Daug,O\text{-}O\text{-}N}$	23%	400%	768%	1010%
	$C_{Daug,O\text{-}O\text{-}O\text{-}N}$	23%	492%	1031%	1412%
	$C_{Daug,blend}$	21%	212%	380%	488%
1.3	$C_{Do,B}$	1.43	1.57	1.59	1.59
	C_{Do1}	2.56	52.60	2540.61	∞
	$C_{Do2,N}$	1.68	1.84	1.87	1.87
	$C_{Do3,O\text{-}N}$	1.74	5.55	8.72	10.84
	$C_{Do4,O\text{-}O\text{-}N}$	1.76	9.73	19.84	27.76
	$C_{Do5,O\text{-}O\text{-}O\text{-}N}$	1.77	12.50	29.66	44.52
	$C_{Do,blend}$	1.73	5.71	10.14	13.49
	$C_{Daug,isentropic}$	79%	3257%	159958%	∞
	$C_{Daug,N}$	18%	18%	18%	18%
	$C_{Daug,O\text{-}N}$	22%	254%	449%	580%
	$C_{Daug,O\text{-}O\text{-}N}$	23%	521%	1150%	1641%
	$C_{Daug,O\text{-}O\text{-}O\text{-}N}$	23%	698%	1768%	2693%
	$C_{Daug,blend}$	21%	264%	539%	746%
1.2	$C_{Do,B}$	1.45	1.60	1.62	1.63
	C_{Do1}	2.72	122.48	29526.00	∞
	$C_{Do2,N}$	1.71	1.88	1.90	1.91
	$C_{Do3,O\text{-}N}$	1.77	6.44	11.50	15.72
	$C_{Do4,O\text{-}O\text{-}N}$	1.80	13.19	34.20	56.13
	$C_{Do5,O\text{-}O\text{-}O\text{-}N}$	1.80	19.30	64.31	119.39
	$C_{Do,blend}$	1.76	7.17	15.87	24.59
	$C_{Daug,isentropic}$	87%	7570%	1823731%	∞
	$C_{Daug,N}$	18%	18%	18%	18%
	$C_{Daug,O\text{-}N}$	22%	303%	610%	867%
	$C_{Daug,O\text{-}O\text{-}N}$	24%	726%	2013%	3352%
	$C_{Daug,O\text{-}O\text{-}O\text{-}N}$	24%	1109%	3872%	7241%
	$C_{Daug,blend}$	21%	349%	880%	1412%

Appendix D: γ_{eff} for Mars

γ, the ratio of specific heats at constant pressure and volume $\left(\frac{C_P}{C_V}\right)$, is constant for calorically perfect gases. At high gas temperatures however, the vibrational energy of the gas molecules becomes excited and the specific heats become functions of temperature.[54] Furthermore, at even higher temperatures chemical reactions (dissociation and ionization) are introduced and the specific heats become functions of both temperature and pressure.[54] Hypersonic flows generally experience these high-temperature effects due to the temperature jumps through shock waves. Thus, complex equilibrium or nonequilibrium codes are necessary to accurately calculate flow characteristics such as γ for high-M_∞ flows.

For simple analysis purposes, however, a constant "effective" γ can be used as an approximation.[46] To determine an effective γ for a simplified hypersonic Mars entry scenario, we used Sutton's SHOCK_MARS9703 code.[55] Given freestream conditions, the code calculates normal shock properties for equilibrium chemistry for a gas made up of 97% CO_2 and 3% N_2 by mass. With the actual density ratio across the shock now known, γ_{eff} is approximated as the γ which would produce this density ratio across a normal shock (the normal shock effective gamma). Solving the normal shock equation

$$\frac{\rho_2}{\rho_1} = \frac{(\gamma+1)M_1^2}{2+(\gamma-1)M_1^2} \tag{45}$$

for γ gives

$$\gamma_{eff} = \frac{\frac{\rho_2}{\rho_1}+1}{\frac{\rho_2}{\rho_1}-1} - \frac{2\frac{\rho_2}{\rho_1}}{\left(\frac{\rho_2}{\rho_1}-1\right)M_1^2} \tag{46}$$

Results are summarized for various altitudes and freestream velocities in Table 7. From this data, it was determined that the typical Mars γ approximation of 1.3 (assuming a calorically perfect gas) breaks down above Mach 5, and that at these hypersonic freestream Mach numbers an effective γ approximation of 1.2 is adequate.

Table 7. γ_{eff} at various conditions.

alt (km)	vel (km/s)	M_∞	γ_{eff}
25	2.0	8.9	1.18
	1.0	4.5	1.24
	0.5	2.2	1.29
10	2.0	8.3	1.18
	1.0	4.2	1.23
	0.5	2.1	1.27